



Sulfide mineralogy of igneous basic rocks (ophites) from the external zone of the Betic Cordillera

José M. González-Jiménez¹, Idael F. Blanco-Quintero², Lola Yesares³, Claudio Marchesi⁴,
Amira R. Ferreira¹, Igor González-Pérez⁴, Erwin Schettino⁵, Francisco Abel Jiménez Cantizano⁶, and
Fernando Gervilla⁴

¹Instituto Andaluz de Ciencias de la Tierra (IACT-CSIC), Avda. de las Palmeras 4,
18100 Armilla, Granada, Spain

²Departamento de Ciencias de la Tierra y del Medio Ambiente, Ciencias 3, Universidad de Alicante, Carretera
San Vicente del Raspeig s/n, 03690 Alicante, Spain

³Departamento de Mineralogía y Petrología, Facultad de Ciencias Geológicas, Universidad Complutense de
Madrid, C/ José Antonio Novais, 12, Ciudad Universitaria, 28040 Madrid, Spain

⁴Departamento de Mineralogía y Petrología, Facultad de Ciencias, Universidad de Granada,
Avda. Fuentenueva s/n, 18002 Granada, Spain

⁵Institute of Geochemistry and Petrology, ETH Zürich, Clausiusstrasse 25, 8092 Zurich, Switzerland

⁶Agencia de Medio Ambiente y Agua, Junta de Andalucía, C/Johan G. Gutenberg, 41092 Seville, Spain

Correspondence: José M. González-Jiménez (jm.gonzalez.j@csic.es)

Received: 25 July 2024 – Revised: 10 January 2025 – Accepted: 12 January 2025 – Published: 20 March 2025

Abstract. The Triassic sedimentary rocks of the external zone of the Betic Cordillera in southern Spain host abundant igneous basic rocks (“ophites”) metamorphosed in the greenschist facies. Investigation based on high-resolution transmission electron microscopy (HRTEM) reveals magmatic sulfides intimately intergrown with primary silicates (pyroxene, plagioclase and olivine), consisting of pyrrhotite (FeS to Fe₇S₈; monoclinic *C2/c* polytype 4C) and pentlandite ((FeNi)₉S₈; cubic *Fm3m*), bounded by tetragonal *I4̄2d* chalcopyrite (CuFeS₂). Whole-rock and clinopyroxene geochemical data suggest that Fe–Ni–Cu sulfides crystallized from melt droplets segregated by immiscibility from transitional-alkaline magmas, after their fractional crystallization and volatile oversaturation within crustal conduits developed during intraplate rifting. In contrast, hydrothermal sulfides are pyrite (FeS₂) and/or chalcopyrite associated with secondary silicates (chlorite, epidote, saussurite, prehnite, sericite and quartz). Porous pyrite (cubic *Pa3*) hosts nanodomains of pyrrhotite (monoclinic *C2/c* polytype 4C and orthorhombic *Cmca* polytype 11C) and orthorhombic *Pnmm* marcasite (FeS₂), evidencing disulfide formation via coupled Fe loss and S addition in pyrrhotite due to reaction with high-*f*S₂ and high-*f*O₂ fluids at < 300 °C. Tetragonal *I4̄2d* chalcopyrite replacing pyrite also preserves nanodomains of pyrrhotite as well as of pyrite / marcasite, suggesting reaction of pre-existing Fe sulfides with Cu transported by low-temperature (~200–100 °C) acidic-to-neutral fluids. Additionally, inclusions of sphalerite (ZnS), galena (PbS) and vaesite (NiS₂) in pyrite and chalcopyrite spotlight metal remobilization during hydrothermal alteration, which is further confirmed by the crystallization of cobaltite coronas (CoAsS) around pyrite. Our new results contribute to the current debate of the full sequence of processes operating in ore-forming mafic systems.

1 Introduction

Hypabyssal (dolerite) and plutonic (gabbro) bodies of basic rocks are among the main hosts for metal sulfides worldwide. In these types of igneous rocks, sulfides are found as accessory minerals, with areas of mineralization and ore deposits that are priority targets for the exploration of economically valuable metals such as Ni, Cu, Co, Au and Ag and the platinum group elements (PGEs) Os, Ir, Ru, Rh, Pt and Pd (Piña, 2019; Neyedley et al., 2019; Mansur et al., 2023). The origin of these sulfides is usually attributed to either magmatic or hydrothermal processes as well as a combination of both. Magmatic sulfides are usually associated with sulfide melt immiscibility in basaltic magmas, and they are usually found as solid inclusions within main minerals such as plagioclase, pyroxene, olivine, and to lesser extent apatite or ilmenite (e.g., Li and Ripley, 2009; Piña et al., 2013; Holwell et al., 2017; Mansur et al., 2023; Neyedley et al., 2019). They are usually the Fe–Ni–Cu sulfides pyrrhotite (Fe_{1-x}S), pentlandite $(\text{Fe,Ni})_9\text{S}_8$, chalcopyrite (CuFeS_2) and bornite (Cu_5FeS_4), corresponding to the low-temperature products of the $(\text{Fe,Ni})_{1\pm x}\text{S}$ monosulfide solid solution (MSS), $[(\text{Cu}_{1\pm x}, \text{Fe}_{1\pm y})\text{S}_2]$ intermediate solid solution (ISS), or the quaternary solid solution spanning the compositional range between heazlewoodite $[(\text{Ni,Fe})_{3\pm x}\text{S}_2]$ ($\text{Hz}_{s,y}$) and ISS (Fleet and Pan, 1994; Li et al., 1996; Ballhaus et al., 2001; Peregoedova and Ohnenstetter, 2002; Naldrett, 2004; Mungall et al., 2005; Helmy et al., 2021). Post-magmatic evolutions of basic rocks may also modify the pre-existing magmatic sulfides via interaction with late magmatic or hydrothermally related metamorphic fluids, promoting the formation of minerals (usually S-poorer sulfides or alloys) that are stable under the new conditions (Mansur et al., 2021) and the further concentration or removal of metals in the rock (Holwell et al., 2017; Wang et al., 2021).

In this work, we address the origin of sulfides in igneous basic rocks from the external zone of the Betic Cordillera in southern Spain (Fig. 1a–b). These rocks include outcrops of small subvolcanic dolerite bodies that were emplaced into sedimentary rocks of marginal basins, mainly during the Triassic–Jurassic limit, and then hydrothermally altered in the Early Miocene by metamorphism related to continental collision (Puga et al., 1988; Morata, 1993; Portugal-Ferreira et al., 1995; Morata et al., 1997; Blanco-Quintero et al., 2024). This is a suitable scenario for evaluating segregation of metal sulfides during magmatism, as well as for elucidating the impact on sulfide mineralogy of fluid–rock interaction during metamorphism. Mineralogical and geochemical data are used to constrain the relative contributions of the “primary” magmatic vs. “secondary” hydrothermal processes, emphasizing the nanoscale study aiming to provide information not accessible by conventional geochemical and mineralogical studies.

2 Geological background

2.1 Geological overview of the Betic Cordillera

The Betic Cordillera is located in southern Spain and constitutes the westernmost segment of the Alpine orogen in the Mediterranean region (Fig. 1a), which was developed by the convergence between the Iberian and African plates from Late Cretaceous to Tertiary times, coeval with the westward migration of the Mesomediterranean subplate (Rosembaum et al., 2002). The Betic Cordillera has traditionally been subdivided into three structural and paleogeographical zones (see Vera, 2004; Fig. 1a): (1) the internal zone (or Alboran domain) is located in the inner arc and consists of remnants of the Mesomediterranean subplate; (2) the external zone (or South Iberian domain) consists of Triassic–Lower Miocene sediments deposited in the south Iberian and northern African paleo-margins, mostly deformed as a fold-and-thrust belt in the outer orogenic arc; and (3) a suture zone is located between the external and internal zones, which comprises the Flysch deposits of the Campo de Gibraltar Complex and the frontal units, both consisting of Cretaceous to Miocene deep-water deposits.

The internal zone extends across the southernmost sector of the Betic Cordillera (Fig. 1a; Vera, 2004). Here, allochthonous tectonic units originally located in the Mesomediterranean paleo-margin (Guerrera et al., 2021) were intensely deformed and metamorphosed, forming an antiformal stack of thick-skinned nappes made of Paleozoic and Meso-Cenozoic rocks that thrust over the southern margin of the Iberian Plate. This antiformal stack comprises three main complexes: (1) the *Nevalo–Filábride Complex*, corresponding to the deepest nappe complex, crops out in several tectonic windows below the overlying Alpujárride Complex in the central and eastern zones of the Betics. It is made up exclusively of metamorphic rocks, which mostly include Paleozoic metasediments (Rodríguez-Cañero et al., 2018) and Permo-Triassic to Cretaceous rocks metamorphosed up to eclogite facies conditions (e.g., Vera, 2004; Puga et al., 2017, and references therein). (2) The *Alpujárride Complex* consists of a lower sequence of metapelites and quartzites of Paleozoic age, an intermediate member of Permian–Middle Triassic phyllites and quartzites with increasing quantities of calc-schists upwards, and an upper variably thick carbonate member of Middle to Upper Triassic age (Martín-Algarra, 1987; Vera, 2004, and references therein). The easternmost lower Alpujárride units contain basic rocks that intruded Permian–Triassic sediments and were metamorphosed during the Alpine collisional (Barrovian) metamorphism (Blanco-Quintero et al., 2024). In the westernmost part of the Betic orogenic belt, the lithological sequence of the Alpujárride Complex includes ultramafic rocks from the subcontinental lithospheric mantle, known as the Serranía de Ronda peridotites. (3) The *Malaguide Complex* comprises Paleozoic sediments unconformably covered by

Permian(?)–Triassic to Lower Miocene sediments that show very low-grade or absent metamorphic overprinting (Vera, 2004; Sanz de Galdeano et al., 2006).

The external zone of the Betic Cordillera crops out widely to the south of the Iberian Cordillera and southeast of the Variscan Massif (Fig. 1a). It is subdivided into two large tectonostratigraphic domains that represent two sectors of the South Iberian paleo-margin (Vera, 2004): (1) the *Prebetic* domain proximal to the Iberian Massif and (2) the more distal *Subbetic* domain. The oldest rocks are Triassic sediments of the Germanic facies (Pérez-López and Pérez-Valera, 2007; Pérez-Valera and Pérez-López, 2008; Pérez-Valera et al., 2017). Younger sediments mainly comprise Middle Triassic (Anisian–Ladinian) epicontinental marine deposits of the Keuper and upper Muschelkalk facies. These deposits constitute the main detachment level of the tectonic units. In particular, the Keuper material consists of multicolored and red shales, sandstones, and gypsum, which are locally intruded by igneous basic rocks that are the subject of this study. These basic rocks were formed during an intracontinental rifting phase affecting the southern Iberian paleo-margin since the Triassic to Middle Jurassic, which has been related to the Central Atlantic Magmatic Province volcanism and the earliest stages of aperture of the Atlantic Ocean (Marzoli et al., 1999; Pérez-López et al., 2021).

2.2 Dolerites (ophites) in the external zone of the Betic Cordillera

More than 2000 outcrops of igneous basic rocks are widespread throughout the internal and external zones of the Betic Cordillera. They include submarine basaltic flows, subvolcanic dolerite and minor gabbro bodies hosted in sedimentary rocks of the Keuper facies (carbonate clays of variegated colors with frequent intercalations of gypsum, marls and carbonates). The K–Ar whole-rock geochronology of basic rocks has yielded ages varying from 187 to 47 Ma (these age endmembers correspond to the localities Alicún de Ortega (Granada Province) and Huelma (Jaén Province; Puga et al., 1988; Morata, 1993; Portugal-Ferreira et al., 1995). Morata (1993) suggested that Cenozoic ages reflect the resetting of older (Triassic or Jurassic) intrusion ages by Alpine metamorphism. The latter event was caused crystallization of secondary quartz, carbonate, amphibole, epidote, pumpellyite, prehnite and chlorite. This assemblage indicates low-grade to very low-grade metamorphism in the prehnite–pumpellyite facies, although minerals suggesting higher-pressure conditions are locally observed (Puga et al., 1983; Morata et al., 1992, 1994; Morata, 1993; Blanco-Quintero et al., 2024).

Overall, the geochemistry of the basic rocks identifies two compositional affinities: (1) tholeiitic and (2) transitional to alkaline sodic (Morata et al., 1997; Pérez-López et al., 2021). The tholeiitic samples are mainly composed of clinopyroxene, plagioclase and minor proportions of orthopyroxene,

while the transitional and alkaline bodies contain olivine in addition to clinopyroxene and plagioclase. These different geochemical signatures point to the generation of magmas from different mantle sources during successive stages of intracontinental rifting affecting the southern Iberian paleo-margin. Continental rifting was related to the early aperture of the Atlantic Ocean in the Triassic to Middle Jurassic (Pérez-López et al., 2021). This syn-rift phase continued in the Late Jurassic–Early Cretaceous and was followed by an Albian to Late Cretaceous passive margin (post-rift) stage (e.g., Morata et al., 1997; Puga et al., 1988; Morata, 1993; Portugal-Ferreira et al., 1995; Pérez-López et al., 2021).

3 Analytical methods

3.1 Sampling

This work focuses on 50 bodies scattered in the external zone of the Betic Cordillera, in an area of around 50×400 km from the Cádiz to Alicante provinces (Fig. 1b). Two hand-specimen samples of each sampled body were cut and sliced into thick polished sections (~ 150 to $200 \mu\text{m}$) in an effort to search for sulfides and other metallic minerals. However, only six clusters of basic bodies had sulfide grains amenable to mineralogical study, all of them hosted in Triassic rocks of the Subbetic zone. These bodies crop out near the town of Alcalá la Real in Jaén Province (Santa Ana and Ermita Nueva in Fig. 1b; Díaz de Neira Sánchez et al., 1988; $37^{\circ}24'46.66''$ N, $3^{\circ}52'27.40''$ W) and the villages of Olvera (toponymic in Fig. 1b; $36^{\circ}54'45.43''$ N, $5^{\circ}21'27.79''$ W), Alcalá de los Gazules (toponymic in Fig. 1b; Hernáiz Huertas et al., 1984; $36^{\circ}27'36.17''$ N, $5^{\circ}43'34.92''$ W), Paterna de Rivera (Peña Arpada in Fig. 1b; $36^{\circ}30'28.97''$ N, $5^{\circ}49'22.03''$ W) and Chiclana de la Frontera (Arroyo del Saltillo in Fig. 1b; García de Domingo et al., 1983; $36^{\circ}25'51.70''$ N, $6^{\circ}1'4.50''$ W) in Cádiz Province.

3.2 Whole-rock geochemistry

Hand-specimen samples were crushed and powdered in an agate mortar and then analyzed for major, minor and trace elements at the Centro de Instrumentación Científica of the Universidad de Granada, Spain. Major element and zirconium compositions were determined on glass beads, made of powdered sample diluted in lithium tetraborate using a Philips MagiX PRO (PW 2440) X-ray fluorescence (XRF) instrument. The precision was better than $\pm 1.5\%$ (relative error) for an analyte concentration of 10 wt% and better than $\pm 0.2\%$ for 5 ppm concentration of Zr. Loss on ignition (LOI) was determined by the weight difference before and after ignition of samples in a furnace. Trace elements, except Zr, were analyzed in the same laboratory by inductively coupled plasma–mass spectrometry (ICP-MS) after $\text{HNO}_3 + \text{HF}$ digestion of 0.1000 g of sample powder in a Teflon-lined vessel at 180°C and 200 psi for 30 min, with evaporation

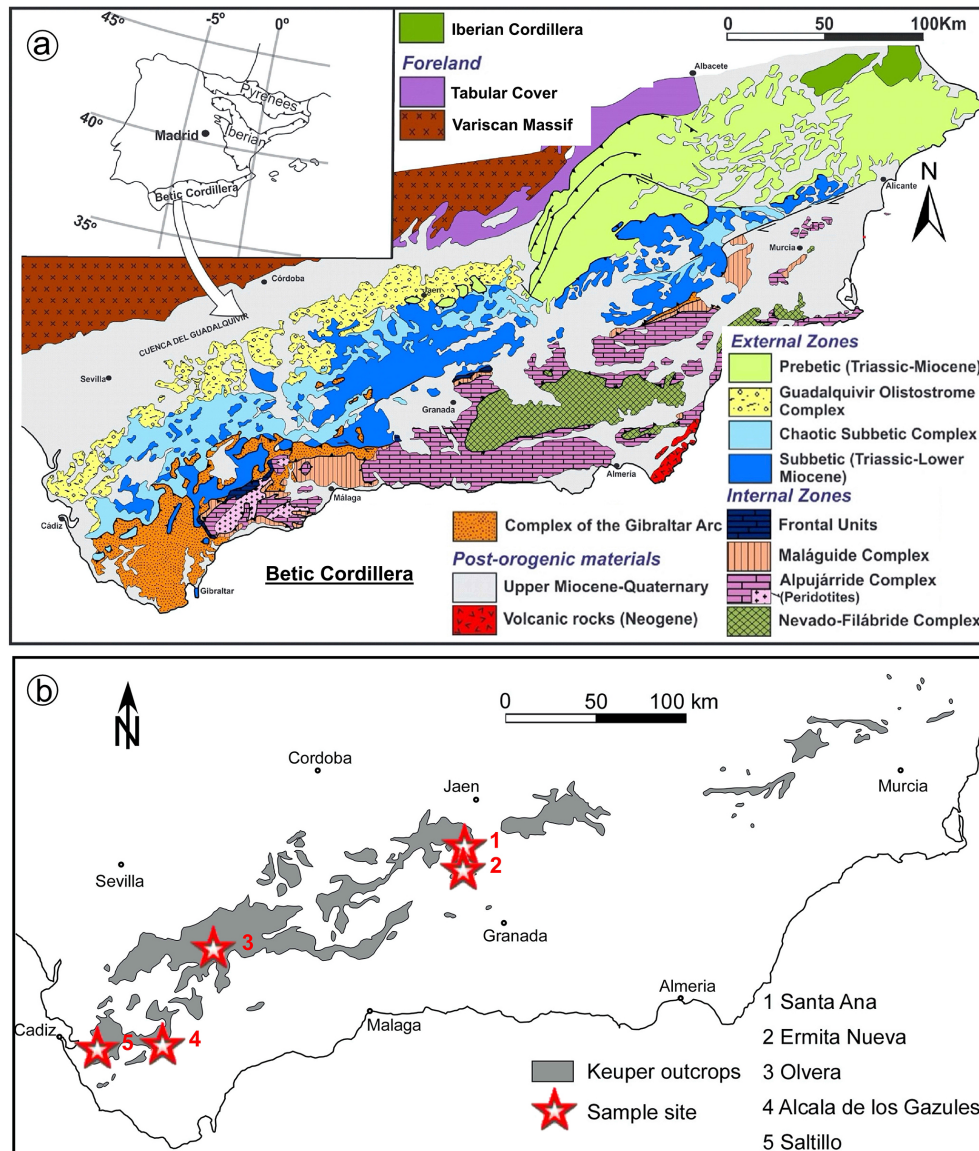


Figure 1. (a) Geological map of the Betic Cordillera (modified from Vera, 2004). (b) Outcrops of sulfide-bearing igneous basic rocks analyzed in this study from the external zone of the Betic Cordillera (modified from Morata, 1993). Legends inset.

to dryness and subsequent dissolution in 100 mL of 4 vol % HNO_3 . The precision was better than $\pm 2\%$ for analyte concentrations of 50 ppm and $\pm 5\%$ for analyte concentrations of 5 ppm. Results of whole-rock analyses are listed in File S1 (Supplement).

3.3 Major, minor and trace element compositions of silicates

Quantitative single-spot analyses of major and minor elements in silicates were carried out by electron probe microanalysis (EPMA) at the Universidad de Huelva (Spain) using a JEOL JXA-8200 SuperProbe equipped with four wavelength-dispersive X-ray spectrometry (WDS) instru-

ments, an energy-dispersive X-ray spectrometer (EDS), and backscattered and secondary electron detectors. Analyses were carried out at very small spot sizes (1–2 μm beam diameter), using an accelerating voltage of 15 kV and a beam current of 20 nA. The standards used were albite (Na), wollastonite (Si and Ca), sanidine (K), rutile (Ti), Al_2O_3 (Al), periclase (Mg), Fe_2O_3 (Fe), Cr_2O_3 (Cr), baryte (Ba), NiO (Ni) and MnO (Mn), and the conventional ZAF correction procedure was applied to the data. Clinopyroxene was normalized to 4 cations and 6 oxygens, with Fe^{3+} estimated by stoichiometry (Morimoto et al., 1988), whereas chlorite was normalized to 11 oxygens. Results of in situ EPMA of silicates are listed in File S2 (Supplement).



Figure 2. Photographs showing field morphologies and structures of some sulfide-bearing dolerite bodies targeted in this study from the Jaén (a) and Cádiz (b–c) provinces. (a) Santa Ana (Alcalá la Real; $37^{\circ}24'46.66''$ N, $3^{\circ}52'27.40''$ W). (b) Arroyo del Saltillo (Chiclana de la Frontera; $36^{\circ}25'51.70''$ N, $6^{\circ}1'4.50''$ W). (c) Alcalá de los Gazules (toponymic; $36^{\circ}27'36.17''$ N, $5^{\circ}43'34.92''$ W).

Trace elements in clinopyroxene were analyzed by laser ablation–inductively coupled plasma–mass spectrometry (LA-ICP-MS). Analyses were conducted on polished thin sections by coupling a Thermo Fisher iCAP RQ ICP-MS instrument and a Teledyne Photon Machines Iridia excimer 193 nm laser at the Andalchron SCT Facility of the Instituto Andaluz de Ciencias de la Tierra, CSIC, Universidad de Granada (Spain). The thin sections were brought into a cobalt cell, supplied with a He gas flow of 0.6 L min^{-1} . During analysis, the laser was fired, employing an energy density of 3 J cm^{-2} with a 10 Hz repetition rate. The integration time for all analyses was 10 or 20 ms depending on the element. The ablation was performed in static spot mode on a $50 \mu\text{m}$ spot size for 40 s as automatic driven positioning. Data were reduced using the Iolite 2.5 software package (Paton et al., 2011) on the Igor Pro platform, by the careful inspection of time-resolved spectra to check for the homogene-

ity and stability of signals during ablation time. Elements were calibrated using the synthetic glass NIST610 SRM. Calcium content, determined by EPMA, was used as an internal standard. The validation standard BHVO-2G (synthetic glass, IAG USGS) was included between the unknowns and shows excellent agreement with working values of this material (Jochum et al., 2016). Results of LA-ICP-MS analyses are listed in File S3 (Supplement).

3.4 Mineralogy of sulfides

Preliminary characterization and imaging of sulfides were carried out using a Leo Gemini field emission scanning electron microscopy (FE-SEM) instrument at the Centro de Instrumentación Científica of the Universidad de Granada, Spain. The instrument was equipped with an energy-dispersive spectra (EDS) detector. The accelerating voltage was 20 kV, and the beam current was optimized for an adequate number of counts for each EDS analysis.

Single-spot analyses of the chemical composition of the sulfides were subsequently acquired using an EPMA (electron probe microanalysis) instrument, a JEOL JXA-8200 SuperProbe at the Servicios Centrales de Investigación of the Universidad de Huelva (Spain). Measurements were performed on carbon-coated polished sections using an accelerating voltage of 20 kV and a beam current of 15 nA. The concentrations of S, Fe, Cu, Co, Ni, Hg, Bi, As, Sb, Se, Zn, Pb and Te were determined by wavelength-dispersive spectroscopy (WDS) in single-spot analyses. Analyzer crystals were PETJ (Sb), PETH (S, Te, Hg, Bi), LIFH (Cu, Ni, Co, Fe) and TAP (As, Se); X-ray lines were $K\alpha$ for S, Fe, Cu, Co, Ni and Zn; $L\alpha$ for Sb, As, Te and Se; and $M\alpha$ for Hg, Bi and Pb. The standard materials were pyrite (S and Fe), native metals (Cu, Co and Ni), HgTe (Hg and Te), Bi_2S_2 (Bi), Zn_3As_2 (As), Sb_2S_3 (Sb), SnSe (Se), ZnS (Zn) and PbS (Pb). Results of EPMA of sulfides are listed in File S4 (Supplement).

Five thin-foil samples (three from Santa Ana plutonic stock and two from Peña Arpada hypabyssal dolerite) were extracted using two focused ion beam scanning electron microscopy (FIB-SEM) instruments at the Servicios Centrales de Investigación Científica y Tecnológica of the Universidad de Cádiz or the Laboratorio de Microscopías Avanzadas (LMA) of the Instituto de Nanociencia de Aragón (INA), Universidad de Zaragoza, Spain. At Cádiz, the transmission electron microscopy (TEM) thin-foil preparation was carried out using an FEI Scios™ 2 DualBeam™, whereas at Zaragoza we employed a Thermo Fisher Scientific FEI DualBeam Helios 650. In the two labs, the selected regions of interest were first covered by a thin strip ($\sim 300 \text{ nm}$) of C by focused-electron-beam-induced deposition (FEBID), and subsequently by a second strip ($\sim 1 \mu\text{m}$) of C in order to avoid potential metal contamination (e.g., by Pt commonly used in this type of sample preparation). These strips act as protection during the milling, polishing and extraction pro-

cess of the thin foils. The bulk material was first removed on both sides of the lamella by rough Ga⁺ ion milling with a 30 kV voltage at 5 nA (Cádiz) and 2.5 nA (Zaragoza) current. The final polishing step was performed until electron transparency was achieved. This was completed by subsequently milling the thin foil with a 5 kV voltage and current at 48 pA (Cádiz) and 68 pA (Zaragoza). The electron transparency was monitored by an Everhart–Thornley secondary electron (SE) detector and using a 5 kV electron beam. After achieving the electron transparency, the thin foil was rapidly polished using a low-energy 5 kV current at 10 pA to reduce the amorphization until a final thin-foil thickness of ~90–70 nm was attained. Subsequently, the thin foil was undercut with a 30 kV voltage at 2.5 nA current, lifted out and transferred from the sample to a TEM grid using an OmniProbe nanomanipulator with a tungsten tip. To weld the thin foil to the tungsten tip and the TEM grid, ion-beam-assisted Pt deposition was performed, ensuring no Pt decoration on the prepared thin foil.

Two high-resolution transmission electron microscopy (HRTEM) instruments were used to analyze the thin foils previously prepared by FIB-SEM: (1) a Thermo Fisher Scientific Talos F200X at the Servicios Centrales de Investigación Científica y Tecnológica of the Universidad de Cádiz (Spain) and (2) a probe-corrected Thermo Fisher Titan TEM instrument equipped with the field emission gun X-FEG at the Laboratorio de Microscopías Avanzadas (LMA) of the Instituto de Nanociencia de Aragón (INA), Universidad de Zaragoza, Spain. The two microscopes are equipped with a high-brightness X-FEG and a spherical aberration Cs corrector (CEOS) at the condenser system (probe-corrected). To characterize the texture of the grains and to properly define the ordering of the mineral aggregates, selected mineral areas of interest sampled within the thin foils were imaged firstly using a combination of high-angle annular dark-field (HAADF) imaging to obtain Z high-contrast images by scanning transmission electron microscopy (STEM) and high-resolution transmission electron microscopy (HRTEM).

The Talos instrument worked at 200 kV accelerating voltage, achieving point resolution ~0.25 and 0.16 nm under the HRTEM and HR-SEM modes, respectively. High-resolution images were obtained using a CMOS Ceta 16 Mpx camera, and the equipment was operated using Velox software. The Titan instrument was run in 300 kV working conditions while HRTEM images were acquired using a Gatan CCD camera. When necessary, post-laboratory filtering of diffraction data acquired by HR image processing (i.e., fast Fourier transform (FFT) images) was carried out using the ImageJ software version 1.543f. In order to analyze the chemical composition of the materials, X-ray energy-dispersive spectra (EDS) were obtained with an Ultim Max detector (Oxford Instruments). All these data were treated using the AZtec Oxford Instruments software package.

A summary of crystallographic data acquired from the thin foils analyzed in this study is provided in Tables A1 and B1 as well as Files S5 and S6 (Supplement).

4 Silicate

4.1 Petrography

Sulfide-bearing dolerites are small bodies < 1 km² (Fig. 2a–c) with textures varying from typical plutonic (in Santa Ana) to hypabyssal (in Ermita Nueva, Olvera, Alcalá de los Gazules, Peña Arpada and Arroyo del Saltillo) (Fig. 3a–g). The Santa Ana stock consists of two layers, one enriched in olivine (up to 45 vol %) at the bottom and another dominated by plagioclase, clinopyroxene and amphibole on the top (Morata and Puga, 1991, 1992). Post-cumulus phases include hydrous minerals such as amphibole (edenite–kaersutite) and phlogopite constituting < 10 vol % of the rock (Fig. 3a–b). In Santa Ana, igneous minerals are relatively well preserved, while in Olvera most primary mineralogy is altered. The hypabyssal dolerites from Ermita Nueva, Alcalá de los Gazules, Peña Arpada and Arroyo del Saltillo are olivine-free and have fine- to medium-grained ophitic to subophitic textures (Fig. 3c–h). The finer-grained rocks occur in chilled margins, while the core of the bodies has a medium grain size. Dolerites show variable degrees of transformation of the original igneous assemblage, mainly clinopyroxene and plagioclase, with no primary silicates preserved in the smaller bodies of Ermita Nueva and Peña Arpada (e.g., Fig. 3c–d). The euhedral to subhedral plagioclase crystals are prismatic and locally embayed against clinopyroxene phenocrysts. Minor proportions of orthopyroxene, biotite and amphibole are present, the latter mainly as a result of transformation of clinopyroxene. Apatite, ilmenite and magnetite are accessory phases. Minor amounts of interstitial quartz and alkali feldspar are locally observed in granophyric intergrowths. Some dolerites include crustal xenoliths (mainly rich in carbonates or sillimanite; Morata and Puga, 1992) and/or are crosscut by quartz veinlets a few millimeters thick. The typical low-temperature metamorphic assemblage of these rocks consists of chlorite ± epidote ± albite ± actinolite ± calcite ± quartz.

4.2 Whole-rock and mineral geochemistry

Whole rocks of the Santa Ana cluster have basic–intermediate compositions with 45.99 SiO₂ wt %–56.12 SiO₂ wt % and total alkali (Na₂O + K₂O) contents of 2.38 wt %–5.15 wt % as well as high Cr (285 ppm) and variable Mg# (51–74) and CaO (6.38 wt %–9.71 wt %) (Fig. 4a; File S1, Supplement). The Olvera olivine-bearing rocks show basic compositions with 48.16 SiO₂ wt %–48.82 SiO₂ wt % and total alkali contents of 4.44 wt %–4.90 wt % but lower Cr (177–211 ppm) and Mg# (58) and higher CaO (9.68 wt %–11.51 wt %) (Fig. 4a). Rocks from these two areas have

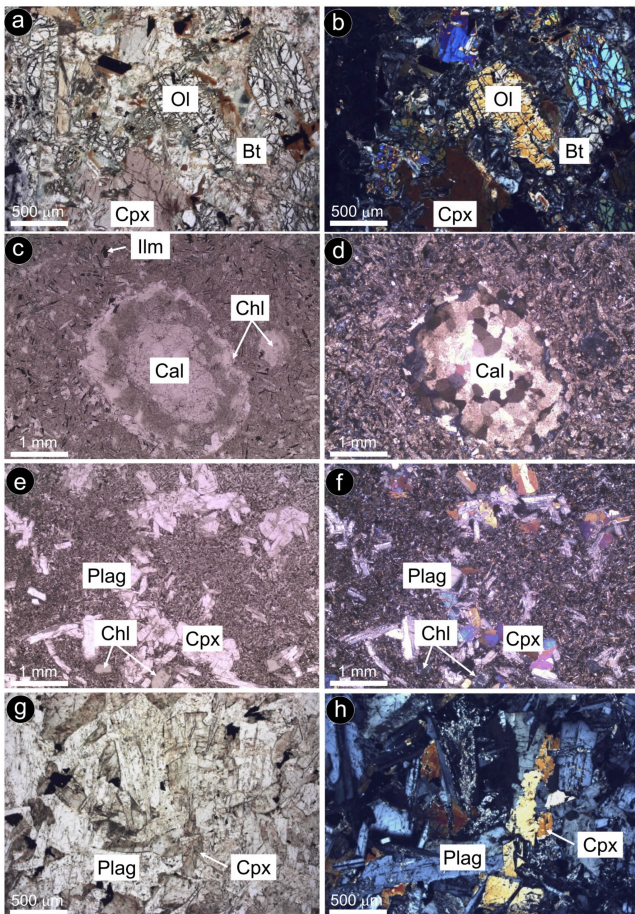


Figure 3. Photomicrographs of selected sulfide-bearing dolerite samples under polarized transmitted light (with both parallel and crossed polarized). (a–b) Olivine-rich cumulate from Santa Ana (Alcalá la Real). (c–d) Xenolith of dolomite + calcite in fully transformed fine-grained dolerite from Ermita Nueva (Alcalá la Real). (e–f) Subophitic texture of partially altered dolerite from Saltillo (Chiclana de la Frontera). (g–h) Ophitic texture of partially altered dolerite from Alcalá de los Gazules. Abbreviations – Ol: olivine; Bt: biotite; Cpx: clinopyroxene; Ilm: ilmenite; Chl: chlorite; Cal: calcite; Plag: plagioclase.

more transitional to alkaline affinities in terms of elements unaffected by low-temperature remobilization (Fig. 4b). Their chondrite-normalized rare earth element (REE) patterns (Fig. 4c) are characterized by a negative slope with strong enrichment in light rare earth elements (LREEs) and depletion in heavy rare earth elements (HREEs) (e.g., $La_N / Yb_N = 3.14–3.35$). In the primitive mantle (PM)-normalized extended trace element diagram (Fig. 4d), these samples show relative enrichment in large-ion lithophile elements (LILEs; Cs, Rb) in comparison with the high-field-strength elements (HFSEs; Nb) and opposite anomalies of Ba, Pb and Sr.

According to Morata (1993), cumulitic olivine from the Santa Ana stock exhibits iron-richer composition

upwards along the profile (Fo_{76–84}), whereas intercumulus plagioclase is mainly labradorite (An_{55–64}) and clinopyroxene is diopsidic (Wo₄₆En₄₄Fs₁₀). The new EP-MAs obtained in this study ($n = 22$; File S2, Supplement) confirm previous results by Morata (1993). Clinopyroxenes from Santa Ana (WSATA-1) have Wo = 46.4–50.0, En = 43.7–48.5, Fs = 3.8–7.1 and Mg# = 86–92, with Al contents = 0.12–0.25 apfu, Ti = 0.03–0.09 apfu and Na = 0.02–0.04 apfu (Fig. 5a–b; Supplement). Clinopyroxenes from Olvera olivine-bearing rocks have compositions with Wo = 48.8–49.8, En = 35.5–37.1, Fs = 13.3–15.6, Mg# = 69–73, Al = 0.25–0.34 apfu, Ti = 0.09–0.10 apfu and Na = 0.04–0.05 apfu (Fig. 5a–b; File S2, Supplement). In situ LA-ICP-MS analyses of the Santa Ana clinopyroxenes yield concentrations of lithophile trace elements varying between ~0.1 and 10, the values of primitive upper mantle (Fig. 5c; Supplement). Normalized patterns show relative depletion in Th, U and Nb and generally increasing contents from Ta to middle rare earth elements (MREEs; e.g., Tb, Dy) (Fig. 5c; File S3, Supplement). Lead, Sr and Eu have notable negative spikes in the normalized patterns (e.g., $Sr_N / Sr^* = 0.2–0.4$, $Sr^* = (Pr_N + Nd_N) / 2$, $Eu_N / Eu^* = 0.7–0.9$, $Eu^* = (Sm_N + Gd_N) / 2$), whereas Ti is slightly enriched compared with adjacent MREEs of similar compatibility. Light and heavy rare earth elements (LREEs and HREEs) are depleted relative to MREEs (e.g., $La_N / Sm_N = 0.4–0.5$, $Sm_N / Yb_N = 1.8–2.2$) (Fig. 5c; File S3, Supplement).

Whole-rock analyses of the olivine-free bodies (Alcalá de los Gazules, Peña Arpada and Arroyo del Saltillo) yield basic–intermediate compositions with 52.96 SiO₂ wt%–53.53 SiO₂ wt% and total alkali (Na₂O+K₂O) contents 4.35 wt%–5.42 wt%, having subalkaline affinities (Fig. 4a–b; File S1, Supplement). These samples have variable Cr (105–178 ppm) and moderate Mg# (48–54) and CaO (8.15 wt%–9.05 wt%). Chondrite-normalized rare earth element patterns (Fig. 4c) are similar to those of Santa Ana and Olvera bodies and show strong enrichment in LREEs relative to HREEs ($La_N / Yb_N = 3.61–3.82$). In the PM-normalized extended trace element diagram (Fig. 4d), these samples also show enrichment in large-ion lithophile elements (LILEs) in comparison with the high-field-strength elements (HFSEs), and Nb is especially depleted (Fig. 4d; File S1, Supplement).

Clinopyroxene in these olivine-free rocks (samples SAL17-3, AG21-4 and AG17-2) is augitic, with Wo = 32.9–45.9, En = 26.4–56.2, Fs = 5.9–30.0, Mg# = 47–90, Ti < 0.03 apfu, Na < 0.02 apfu and Al < 0.12 apfu (Fig. 5a–b; File S2, Supplement). In situ LA-ICP-MS analyses show lower trace element contents than in the Santa Ana dolerite (~0.02 to 4, the values of primitive upper mantle; Fig. 5c; File S3, Supplement), except for Ba, Th, U and Nb with concentrations variable between 1–2 orders of magnitude, possibly reflecting ablation of low-temperature epidote and/or amphibole inclusions. Normalized patterns of these clinopyroxenes show evident negative spikes

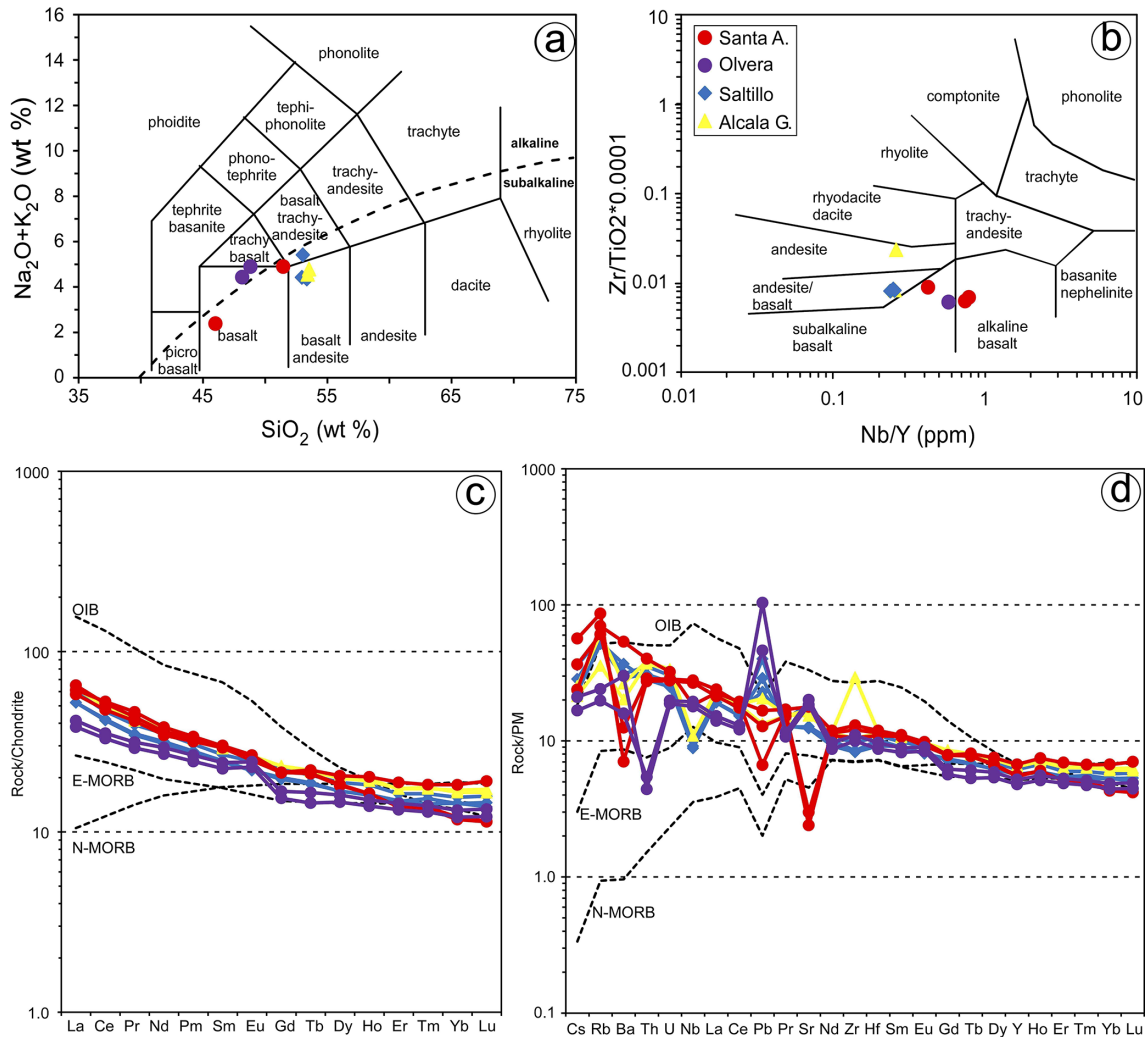


Figure 4. Bulk-rock composition of analyzed samples. **(a)** Total alkali silica (TAS) diagram of Cox et al. (1979; the red line divides the alkaline and subalkaline fields). **(b)** Zr / TiO₂ versus Nb / Y classification diagram of Winchester and Floyd (1977). Chondrite-normalized (McDonough and Sun, 1995) REE patterns **(c)** and N-MORB-normalized (Sun and McDonough, 1989) trace element patterns **(d)** of the samples. The compositions of N-MORB, E-MORB and OIB (Sun and McDonough, 1989) are plotted for reference.

of Pb and Sr, although spikes of Pb are less prominent than in clinopyroxene from Santa Ana (Fig. 5c; File S3, Supplement). Zirconium and Hf are notably fractionated relative to LREEs and MREEs (e.g., $Zr_N / Nd_N = 0.1\text{--}0.4$ in Alcalá de los Gazules and Saltillo vs. $0.6\text{--}0.9$ in Santa Ana), and Ti is generally depleted compared to MREEs (Fig. 5c; File S3, Supplement). Concentrations of LREEs and Eu are variably fractionated relative to MREEs ($La_N / Sm_N = 0.3\text{--}1.3$, $Eu_N / Eu^* = 0.8\text{--}1.3$), and MREEs and HREEs are less fractionated than in Santa Ana clinopyroxene ($Sm_N / Yb_N = 1.0\text{--}1.5$).

5 Sulfide mineralogy

The proportions of sulfides vary from one dolerite body to another between ~ 1 vol % and 10 vol %. The sulfide assem-

blage mainly consists of phases rich in Fe (pyrite, marcasite, pyrrhotite), Fe–Ni (pentlandite and vaesite) or Cu (chalcopyrite and bornite). These minerals are associated with both primary igneous and alteration-related (secondary) silicates.

5.1 Micrometer-scale to nanoscale characterization of sulfides associated with primary igneous silicates

Fe–Ni–Cu sulfides intimately associated with primary igneous silicates of the dolerite were exclusively identified in the small intrusive stock of Santa Ana (Figs. 6 and 7). Here, the Fe–Ni–Cu sulfides (up to 10 vol %) are disseminations between cumulus minerals (pyroxene, plagioclase and olivine) or post-cumulus hydrous silicates such as biotite (partially transformed to chlorite), ilmenite and apatite (Fig. 6). They consist of grains up to 2 cm in size made up

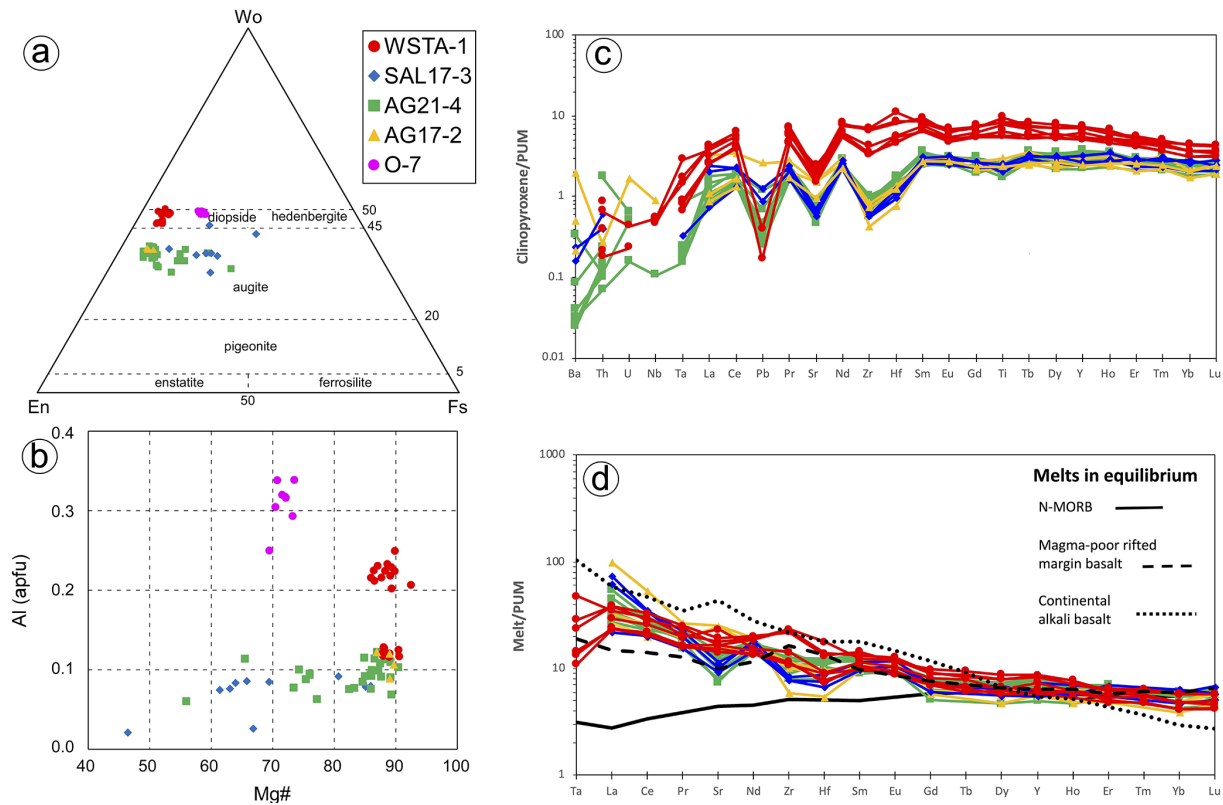


Figure 5. In situ geochemistry of clinopyroxene in the sulfide-bearing dolerites of this study. (a–b) Major elements obtained by EPMA (using classification scheme of Morimoto et al., 1998). (c) Minor and trace elements obtained by LA-ICP-MS. Note that in (d) melts in equilibrium with clinopyroxene from the Santa Ana olivine-rich dolerite stock were calculated applying the partition coefficients of Bonechi et al. (2021) between diopside and alkali basalts (Ta: 0.06; La: 0.11; Ce: 0.19; Pr: 0.29; Sr: 0.104; Nd: 0.41; Zr: 0.30; Hf: 0.62; Sm: 0.65; Eu: 0.54; Gd: 0.78; Tb: 0.87; Dy: 0.90; Y: 0.85; Ho: 0.86; Er: 0.86; Tm: 0.77; Yb: 0.76; Lu: 0.75), whereas melts in equilibrium with clinopyroxene from olivine-free hypabyssal dolerites of Alcalá de los Gazules and Arroyo del Saltillo were computed applying the partition coefficients of Norman et al. (2005) between high-Ca augite and tholeiitic melts (La: 0.033; Ce: 0.065; Pr: 0.105; Sr: 0.061; Nd: 0.155; Zr: 0.072; Hf: 0.141; Sm: 0.270; Eu: 0.271; Gd: 0.377; Dy: 0.467; Y: 0.444; Ho: 0.500; Er: 0.425; Yb: 0.438; Lu: 0.418). Representative compositions of N-MORB (solid line; Klein, 2003), basalt from magma-poor rifted margins (dashed line; Desmurs et al., 2002) and continental alkaline basalts (dotted line; Farmer, 2003) are shown for comparison. Normalizing values are from Sun and McDonough (1989). PUM denotes primitive upper mantle.

of single, biphasic or polyphase aggregates of pyrrhotite $[\text{Fe}_{1.00}\text{S}_{1.00}$ to $\text{Fe}_{0.98}\text{Cu}_{0.015}\text{Ni}_{0.05}\text{S}_{1.00}] \pm$ pentlandite $[(\text{Fe}_{4.52}\text{Ni}_{4.27}\text{Co}_{0.14})_{\Sigma=8.93}\text{S}_{8.07}$ to $(\text{Fe}_{4.75}\text{Ni}_{4.07}\text{Co}_{0.08}\text{Cu}_{0.01})_{\Sigma=8.91}\text{S}_{8.09}] \pm$ chalcopyrite $[\text{Cu}_{0.97}\text{Fe}_{1.01}\text{S}_{2.01}$ to $\text{Cu}_{0.99}\text{Fe}_{0.98}\text{S}_{2.02}] \pm$ magnetite (Fig. 6; File S4, Supplement). These sulfides have globular-like morphologies, including droplet, lobate, cusped and holly leaf (Fig. 6). Within the larger composite blebs, pentlandite has four different textures: granular (Pn-1), granular with marginal blades (Pn-2), fans (Pn-3) and flames (Pn-4) (Figs. 6 and 7).

As illustrated by the X-ray maps of Fig. 7, granular pentlandite (Pn-1) is commonly located around the margins of pyrrhotite and at the contact with chalcopyrite, where it may form loop or rim textures. In contrast, chalcopyrite is found as laths within oriented fractures in pyrrhotite or more frequently forming the outer portion of the composite aggregates.

The nanoscale study targeted the globular-like sulfide assemblage of pyrrhotite–pentlandite–chalcopyrite shown in Fig. 6e. We extracted three thin foils that sampled two types of granular pentlandite (Pn-1 and Pn-2) as follows: (1) perpendicular to the contact between granular pentlandite with marginal blades (Pn-2) and pyrrhotite (thin foil 1; Fig. 8b), (2) within granular pentlandite (Pn-1) (thin foil 2; Fig. 8c), and (3) perpendicular to the contact of granular pentlandite (Pn-1) with chalcopyrite (thin foil 3; Fig. 8d).

The STEM images and EDS–STEM maps collected from thin foil 1 are fully consistent at depth with the micrometer-sized structure observed on the grain surface. Thus, a sharp contact between Ni-free pyrrhotite and pentlandite is revealed by contrasting differences in S, Fe and overall Ni contents (Figs. 8b1 and 9a–b). At higher magnification, the HRTEM image shows that the contact is abrupt even in the nanoscale realm without a scalloped boundary and is marked

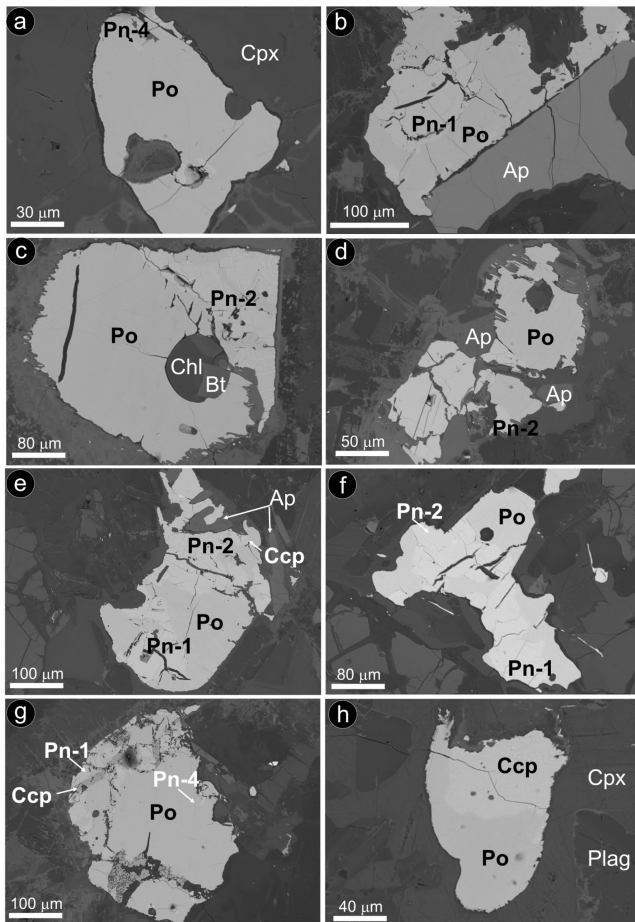


Figure 6. Backscattered electron images of selected sulfide grains associated with unaltered magmatic silicates from the Santa Ana olivine-rich dolerite stock. **(a)** Sulfide bleb fully hosted in primary clinopyroxene. **(b–h)** Sulfide blebs intercumulus to magmatic olivine and clinopyroxene. Abbreviations – Po: pyrrhotite; Pn: pentlandite; Ccp: chalcopyrite; Cpx: clinopyroxene; Plag: plagioclase; Ap: apatite; Chl: chlorite; Bt: biotite. Textural types of pentlandite correspond to granular (Pn-1), granular with marginal blades (Pn-2), fans (Pn-3) and flames (Pn-4).

by a perfectly incoherent interface where the lattice fringes of pyrrhotite and pentlandite display distinctively different orientations with a high-angle misfit (Fig. 9b). This incoherency of the crystallographic orientation relationship (COR) is also illustrated by the contrasting brightness in HRTEM images of the two minerals, evidencing different tilts between the crystallographic axes. The well-defined single-spot and annular patterns observed in the corresponding FFT image (Fig. 9b1) evidence the polycrystalline nature of both mineral matrices. Moreover, the identification of similar nanoscale features far away from their mutual contact suggests that the polycrystalline nature of both crystals is not related to lattice distortion in the proximities of the grain interface.

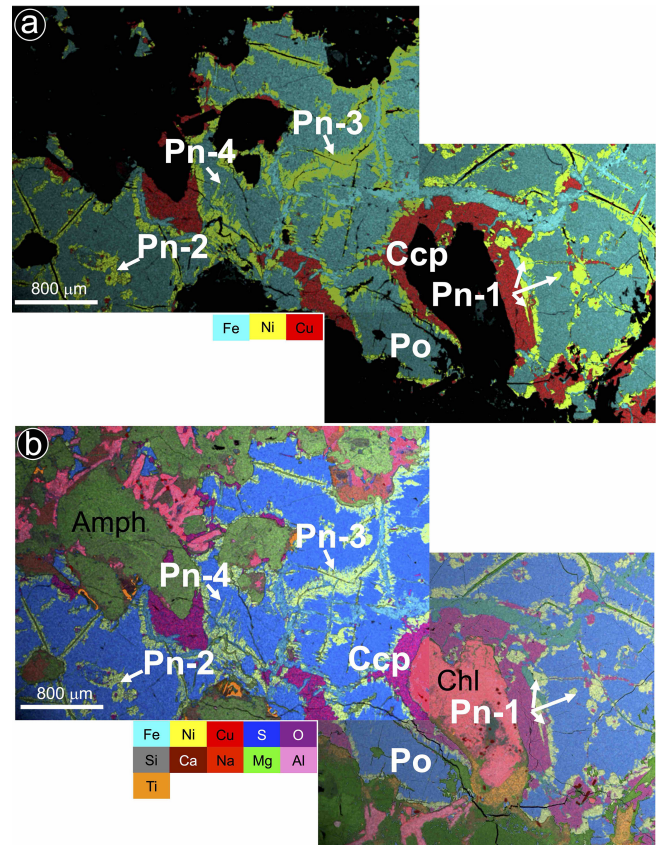


Figure 7. **(a–b)** X-ray images showing the textural and compositional feature of a large intercumulus Fe–Ni–Cu sulfide aggregate in the olivine-rich Santa Ana dolerite stock. Abbreviations – Po: pyrrhotite; Pn: pentlandite; Ccp: chalcopyrite; Amph: amphibole; Chl: chlorite. Textural types of pentlandite correspond to granular (Pn-1), granular with marginal blades (Pn-2), fans (Pn-3) and flames (Pn-4).

Crystallographic data collected from the pyrrhotite–pentlandite interface yield measured d spacings typical of the monoclinic (space group $C2/c$) polytype 4C of pyrrhotite (hereafter pyrrhotite-4C), and the cubic $Fm\bar{3}m$ structure of pentlandite (Fig. 9; Table A1 and File S5 in the Supplement). Pyrrhotite crystals exhibit lattice fringes of the aforementioned cubic $Fm\bar{3}m$ pentlandite (File S5, Supplement), as well as of tetragonal $I\bar{4}2d$ chalcopyrite and cubic $F\bar{4}3m$ bornite (Fig. 9; Table A1 and File S5 in the Supplement). In contrast, pentlandite only hosts lattice fringes of tetragonal $I\bar{4}2d$ chalcopyrite.

The nanoscale study of thin foils 2 and 3 shown in Fig. 8c–d was limited to STEM analysis because we noted visible evidence of changes during the FIB sample preparation, attributable to mechanical and physical–chemical causes. These artifacts were apparently introduced by mechanical deformation and curling of lamellar material during cutting–milling–lifting–attaching–thinning, very likely causing activation of pre-existing fractures not visible on the mineral sur-

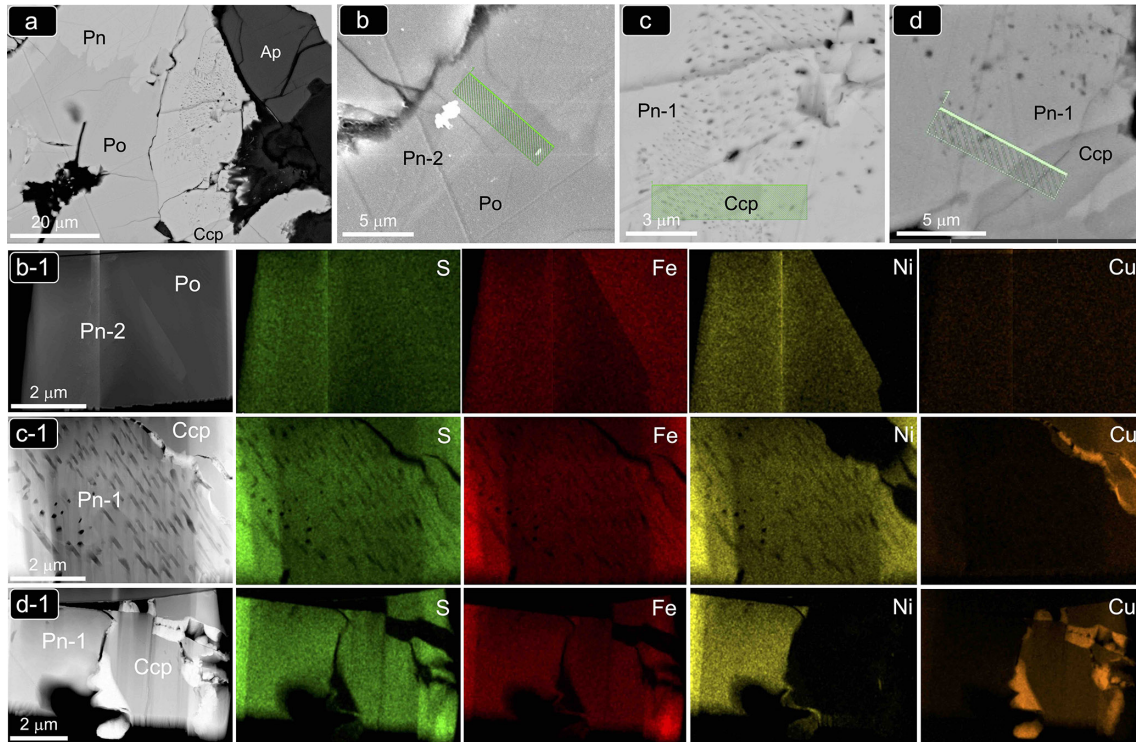


Figure 8. (a–d) Backscattered electron (BSE) images of the magmatic Ni–Fe–Cu sulfide aggregate from the Santa Ana olivine-rich dolerite stock shown in Fig. 6e. Bright-field (BF) HAADF images and corresponding EDS–STEM chemical maps of the FIB thin foils extracted from this sulfide aggregate are shown in (b1), (c1) and (d1). Abbreviations – Po: pyrrhotite; Pn: pentlandite; Ccp: chalcopyrite; Ap: apatite.

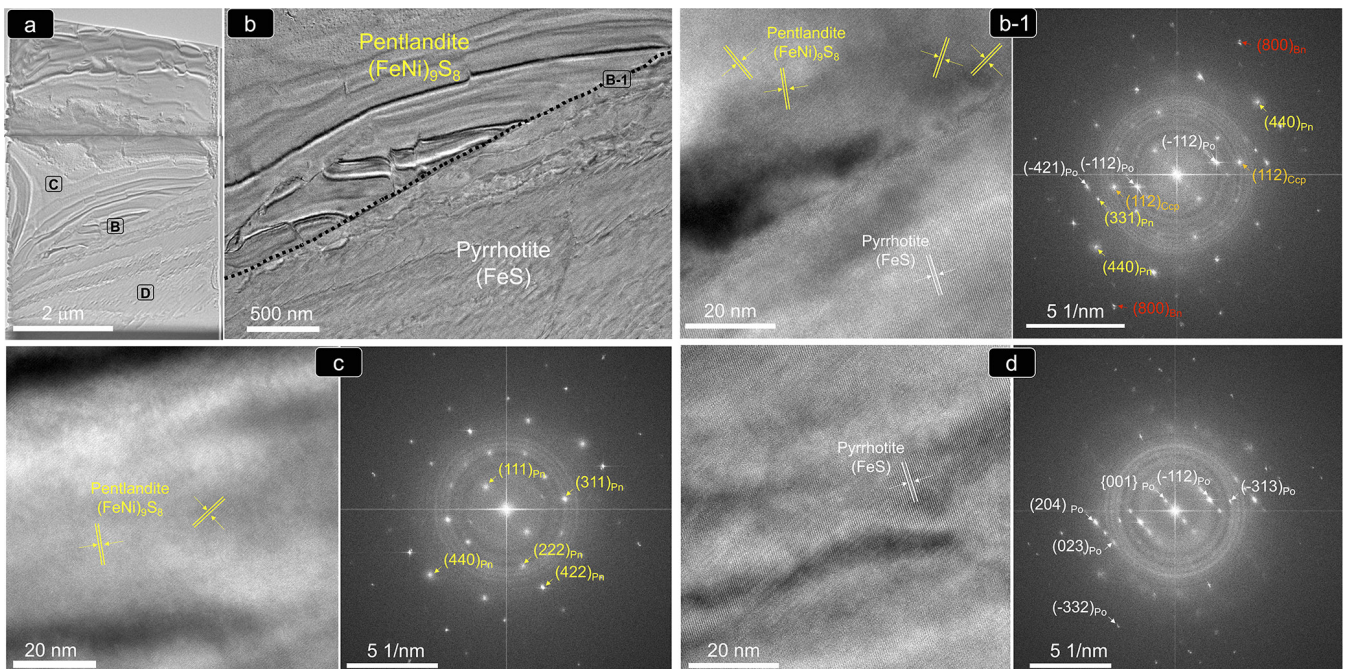


Figure 9. (a–d) (HR)TEM images and corresponding FFT patterns of thin foil 1 shown in Fig. 8b1. Abbreviations – Po: pyrrhotite; Pn: pentlandite; Ccp: chalcopyrite; Bn: bornite.

face by means of FE-SEM. The STEM images and EDS-STEM maps collected from thin foil 2 allow identification of a chalcopyrite particle within granular pentlandite (Pn-1) hosting a crew of decrepitated melt–fluid inclusions. Unlike on the grain surface, the deep contact between chalcopyrite and pentlandite consists of a fracture, which very likely originated during FIB preparation. Similar obliteration of the original relationships between Pn-1 and chalcopyrite is also observed in thin foil 3. Here, the contact of a relatively homogenous pentlandite grain (Pn-1) with chalcopyrite was distorted and fractured, producing areas with distinctively different thicknesses. Thicker zones in the chalcopyrite grain produced higher intensity in the map of Cu abundance, which is not due to chemical variations.

5.2 Micrometer-scale to nanoscale characterization of sulfides associated with partially altered silicates

Pyrite and chalcopyrite are associated with partially altered and secondary (metamorphic) silicates of both olivine-bearing (Olvera) and olivine-free (Ermita Nueva, Arroyo del Saltillo, Peña Arpada and Alcalá de los Gazules) dolerites (Fig. 10a–h). They form single and composite grains (from a few micrometers to several millimeters in size) that are either included in or interstitial between partially altered primary silicates (olivine, pyroxenes and plagioclase). Pyrite $[\text{Fe}_{0.91}\text{Co}_{0.03}\text{Ni}_{0.02}\text{S}_{2.03}\text{As}_{0.01} \text{ to } \text{Fe}_{1.00}\text{S}_{1.00}]$ displays an anhedral shape with spongy internal texture and weak anisotropy in reflected light (Fig. 10a–g; File S4, Supplement). In places, pyrite is intergrown with quartz, filling late fractures (Fig. 10h). Chalcopyrite $[\text{Cu}_{0.86}\text{Fe}_{1.00}\text{Co}_{0.02}\text{S}_{2.12} \text{ to } \text{Cu}_{0.95}\text{Fe}_{1.02}\text{S}_{2.02}]$ forms single grains randomly dispersed in the altered silicate matrix or more commonly replacive rims around the porous pyrite (Fig. 10c–g; File S4, Supplement).

Careful inspection by FE-SEM shows abundant solid inclusions ($< 5 \mu\text{m}$) of chalcopyrite hosted in pores infilled by secondary quartz \pm epidote \pm goethite (Fig. 11a–b). In contrast, large chalcopyrite grains typically host sphalerite and galena along with apatite (Fig. 11c–f). Cobaltite $[\text{Co}_{0.76}\text{Ni}_{0.07}\text{Fe}_{0.10}]_{\Sigma=0.93}\text{S}_{1.11}\text{As}_{0.97}$ to $(\text{Co}_{0.81}\text{Ni}_{0.10}\text{Fe}_{0.09})_{\Sigma=1.01}\text{S}_{1.05}\text{As}_{0.94}$ occasionally forms rims wrapping pyrite grains (Fig. 11g–h; File S4, Supplement).

The nanoscale study was performed on two thin foils cut perpendicular to micrometer-sized chalcopyrite inclusions hosted in the pores of a single large pyrite grain, which were interstitially between plagioclase ghosts from the strongly altered Peña Arpada body (Fig. 12a–e).

The STEM and HRTEM images and EDS-STEM maps collected from thin foil 1 (Figs. 12 and 13) confirm that the chalcopyrite micro-inclusion is fully embedded in a matrix of iron oxide intimately intergrown with quartz. Crystallographic data collected from this chemically homogeneous chalcopyrite micrometer-sized inclusion allow identifi-

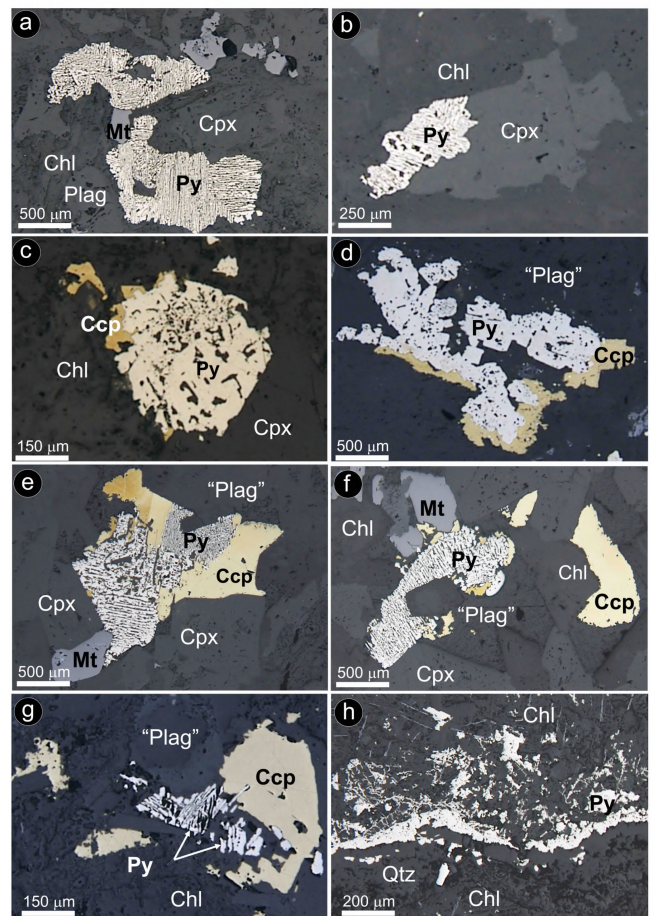


Figure 10. Photomicrographs under reflected-light microscope (parallel nicols) of representative pyrite \pm chalcopyrite assemblages in hydrothermally altered olivine-free hypabyssal dolerites. (a–b) Alcalá de los Gazules. (c–d) Olvera. (e–f) Arroyo del Saltillo. (g) Peña Arpada. (h) Ermita Nueva. Abbreviations – Py: pyrite; Ccp: chalcopyrite; Mt: magnetite; Cpx: clinopyroxene; Plag: plagioclase; “Plag”: saussurite plagioclase; Chl: chlorite; Qtz: quartz.

cation of the planes (112) and (224) of the tetragonal $\bar{1}42d$ form of chalcopyrite (Fig. 13d; Table B1 and File S6 in the Supplement). The HRTEM inspection of the iron oxide matrix shows that it developed at the expense of pyrite, through its interface with quartz (Fig. 13a–d). The FFT patterns collected from this iron oxide matrix identify crystalline goethite with the following characteristic planes: {111}, (130), (200), (210), (212) and (240) (Table B1 and File S6 in the Supplement). Likewise, HRTEM and FFT images of pyrite in the matrix also show a crystalline nature, typified by the coexistence of the characteristic planes (111), (112)/(221) and (311) of pyrite, with abundant lattice fringes of marcasite (e.g., $(202)_{\text{py}}/(121)_{\text{mc}}$, $(222)_{\text{py}}/(130)_{\text{mc}}$ and $(302)_{\text{py}}/(131)_{\text{mc}}$; Fig. 13; Table B1 and File S6 in the Supplement).

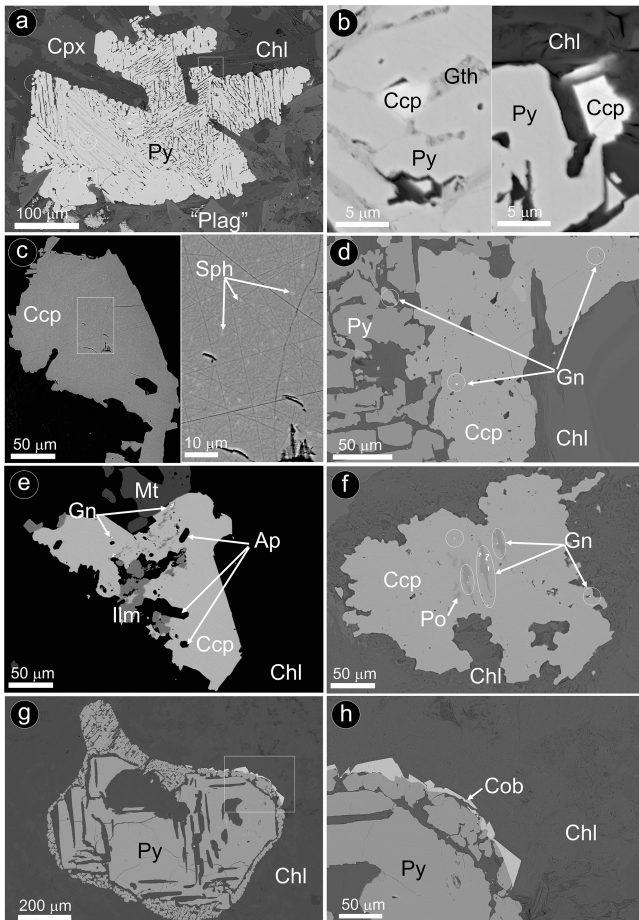


Figure 11. BSE images of representative pyrite ± chalcopyrite assemblages hosting nano- to micrometer-sized inclusions of chalcopyrite, sphalerite and galena as well as rims of cobaltite in hydrothermally altered olivine-free hypabyssal dolerites. (a–f) Peñá Arpada. (g–h) Arroyo del Saltillo. Abbreviations – Po: pyrrhotite; Py: pyrite; Ccp: chalcopyrite; Sph: sphalerite; Gn: galena; Cob: cobaltite; Mt: magnetite; Cpx: clinopyroxene; “Plag”: saussurite plagioclase; Chl: chlorite; Gth: goethite; Ap: apatite; Ilm: ilmenite.

Moreover, the analysis of areas relatively enriched in Fe and depleted in S in the pyrite–marcasite matrix reveals nanodomains of pyrrhotite with both monoclinic $C2/c$ polytype 4C and orthorhombic $Cmca$ polytype 11C structures (Figs. 12d and 13c; Table B1; File S6, Supplement). On the other hand, HRTEM observation of quartz shows structural and chemical homogeneity of a monocrystal yielding measured d spacings typical of the alpha-quartz, or low quartz (Fig. 13a; Table B1; File S6, Supplement).

The STEM and HRTEM images and EDS–STEM maps collected from thin foil 2 show that the chalcopyrite inclusion is in direct contact with a pyrite matrix hosting marcasite fringe (Figs. 12 and 14; File S6, Supplement). Thus, the goethite halo is limited to the deepest portion. The EDS–STEM images also reveal chemical heterogeneity in terms of S, Cu, Co and Ni within the chalcopyrite inclusion, which

is also observed by brightness contrast in the HAADF image (Fig. 12e). These variations are related to patchy Cu–Fe zoning, as well as to the presence of the minute inclusion of a Ni–Co sulfide not observed on the surface. The FFT patterns also evidence the tetragonal $\bar{1}42d$ form of chalcopyrite hosting an inclusion of vaesite (Fig. 14c–d and File S6 in the Supplement).

6 Discussion

6.1 Magmatic segregation of Ni–Fe–Cu sulfide melts in olivine-bearing dolerites

Sulfides in the Santa Ana dolerite stock form disseminated globular aggregates within primary magmatic silicates or at their interstices (Fig. 6). This intimate intergrowth with silicates supports a genetic link to magmatic processes that formed their hosting minerals.

Morata and Puga (1992) suggested that the Santa Ana dolerite stock crystallized from a basaltic melt derived from an enriched mantle source that partially melted during continental rifting. The high Mg# of olivine and the high concentrations of trace elements in clinopyroxene, coupled with the prominent negative anomalies of Pb, Sr and (to a lesser extent) Eu in the latter (Fig. 5c), suggest that the parental melt substantially fractionated olivine and plagioclase prior to clinopyroxene. Clinopyroxene in the Santa Ana dolerite is Ti–Na-rich diopside (Fig. 5a; File S2, Supplement), thus supporting the transitional-alkaline affinity of its parental melt (Portugal-Ferreira et al., 1995; Morata et al., 1997). In addition to fractional crystallization, the high concentrations of trace elements and MREE / HREE fractionation of this clinopyroxene (Fig. 5c) support the claim that transitional-alkaline parental magmas derived by low degrees of melting of an enriched lithospheric mantle started to melt in the garnet peridotite facies (> 70 km depth). Melting of the lithospheric mantle likely occurred during the early stages of continental rifting associated with asthenosphere upwelling (Pérez-López et al., 2021). The calculated compositions of melts in equilibrium with the Santa Ana diopside reinforce these conclusions, as they resemble those of basalts with alkaline affinity from magma-poor continental rifted margins (Fig. 5d). In such a tectonic setting, intraplate basalts are extracted from deep mantle sources by low rates of partial melting at relatively low fO_2 , thus being saturated or close to saturation in sulfide when they leave the mantle source (Kovalenko et al., 2007; Sun et al., 2020; Liu et al., 2021). Therefore, they should have enough sulfur content at sulfide saturation (SCSS) to separate sulfide melts by simple fractional crystallization (e.g., Seat et al., 2009). However, the local relation of the Fe–Ni–Cu sulfides to hydrous silicates (amphibole, phlogopite and biotite; Fig. 6) in Santa Ana supports that increase in $aSiO_2$ and fS_2 took place concomitantly with the accumulation of volatiles. Sulfur originally present in the silicate melt as H_2S may have exsolved

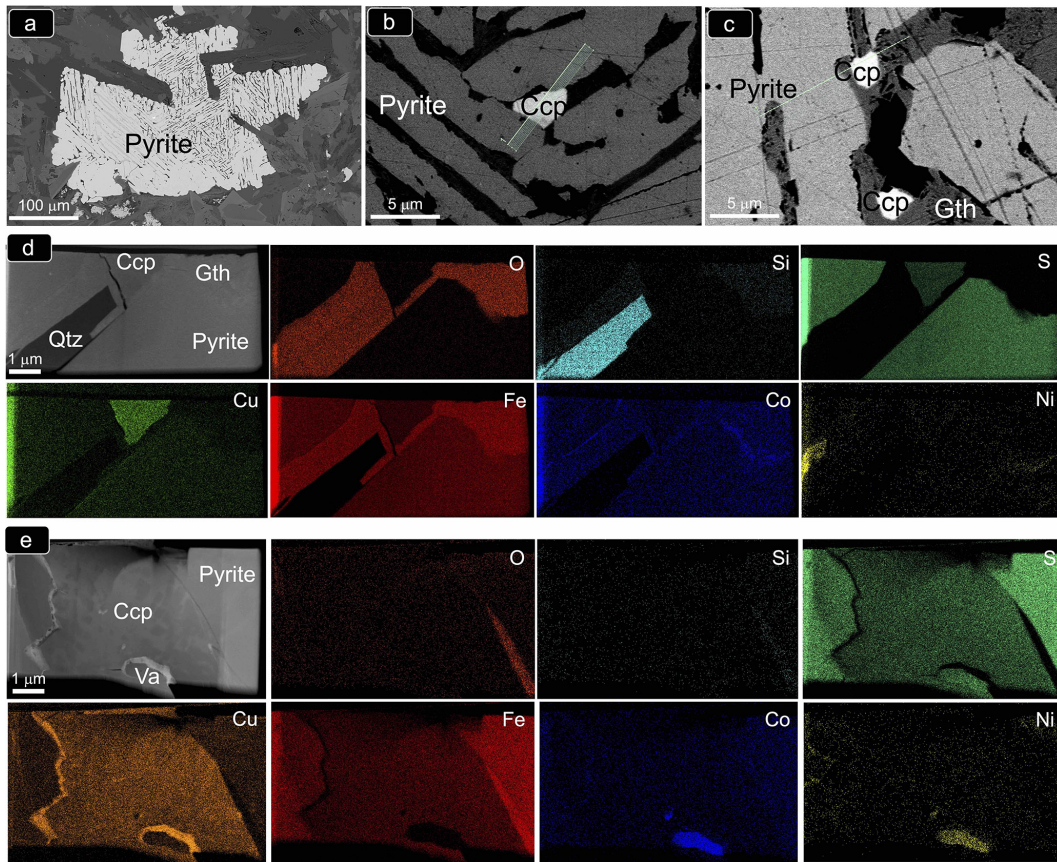
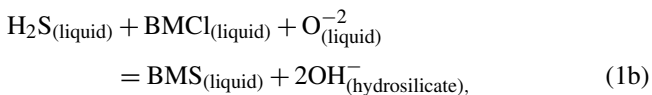
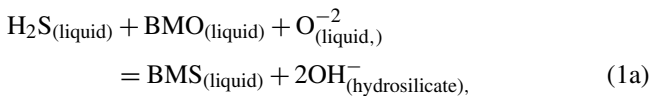


Figure 12. (a–c) BSE images of porous pyrite from the olivine-free hypabyssal dolerite of Peña Arpada shown in Fig. 11a. BF HAADF images and corresponding EDS–STEM chemical maps of the FIB thin foils extracted from this sulfide aggregate are shown in (d) (thin foil 1) and (e) (thin foil 2). Abbreviations – Ccp: chalcopyrite; Gth: goethite; Qtz: quartz; Va: vaesite.

as metal-rich immiscible sulfide liquid, via the reactions between H_2S , base metal oxide and (Cl, F, OH, CO) complexes (e.g., Ferrario and Garuti, 1990):



where BMO is base metal oxide, BMCl is base metal chloride and BMS is base metal sulfide.

Upper-crustal conduits (pipes, dikes and sills) for basic magmas, similar to those developed during continental break-up in Triassic sediments of the external Betic Cordillera (Fig. 15; Morata, 1993; Pérez-López et al., 2021), are favorable structures for the immiscible segregation of sulfide melts. In Santa Ana, the observation of xenoliths of gypsum-rich clays and carbonaceous metapelites (Morata and Puga, 1992) suggests that segregation of sulfide melts was likely aided by supply of S and SiO_2 via assimilation of the country rocks (Ripley and Li, 2013). Sulfide

droplets flushing out to higher levels of the magmatic plumbing system was possibly aided by volatile-rich bubbles that originated from oversaturation after the crystallization of the lower olivine-rich cumulate layer (Mungall et al., 2015; Blanks et al., 2020). However, the small volume of sulfides in the rock and their low average S/Se ratio (~ 2400 ; File S4, Supplement) overlapping the typical range of mantle sulfides (2000–4000; Durand et al., 2016) pinpoints very limited crustal contamination of the parental magma.

6.2 Crystallization sequence of magmatic Ni–Fe–Cu sulfides

Geothermometry of pyroxenes yields crystallization temperatures of the Santa Ana dolerite stock at ~ 1175 – 1150 °C (Morata, 1993). According to the condensed phase diagrams, slightly below these temperatures (~ 1100 °C) the first solid crystallizing from a Fe–Ni–Cu sulfide melt is the monosulfide solid solution (i.e., MSS; $\text{Fe}_{1\pm x}\text{S}$ to $\text{Ni}_{1\pm x}\text{S}$) (Fig. 16a). Experiments in the quaternary (Fe–Ni–Cu–S) and ternary systems (Fe–Cu–S and Fe–Ni–S) show that MSS may coexist with Cu–Fe–(Ni) sulfide melt at ~ 900 °C (Fig. 16b). In

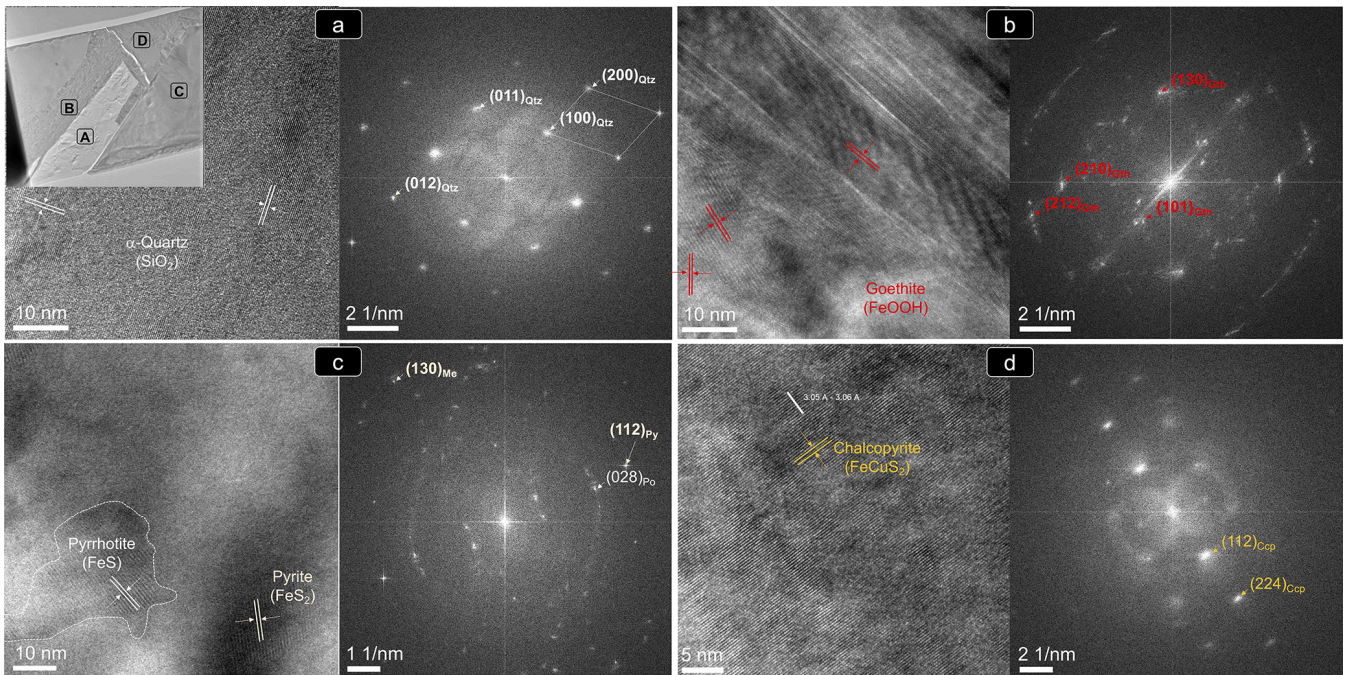


Figure 13. (HR)TEM images and corresponding FFT patterns of thin foil 1 shown in Fig. 12d. (a–d) Locations targeted for the nanostructural study. Abbreviations – Py: pyrite; Mc: marcasite; Po: pyrrhotite; Ccp: chalcopyrite; Gth: goethite; Qtz: quartz.

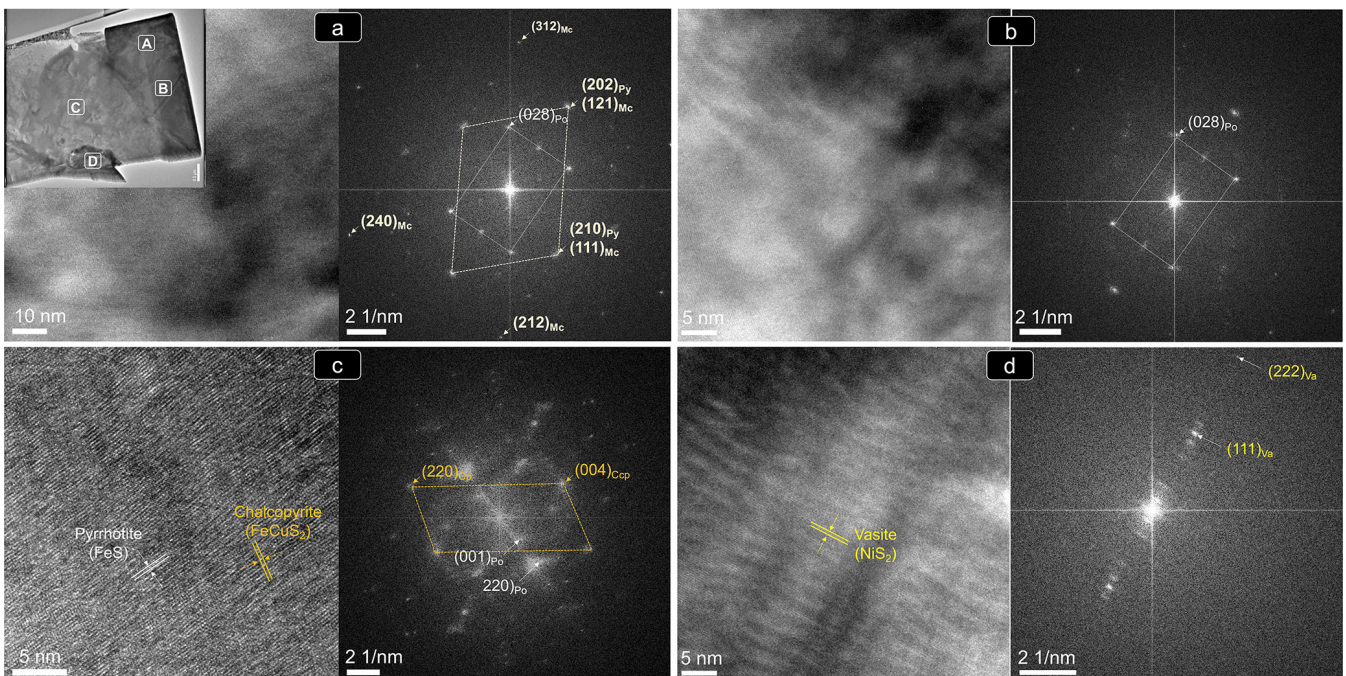


Figure 14. (HR)TEM images and corresponding FFT patterns of thin foil 1 shown in Fig. 12e. (a–d) Locations targeted for the nanostructural study. Abbreviations – Py: pyrite; Mc: marcasite; Po: pyrrhotite; Ccp: chalcopyrite; Va: vaesite.

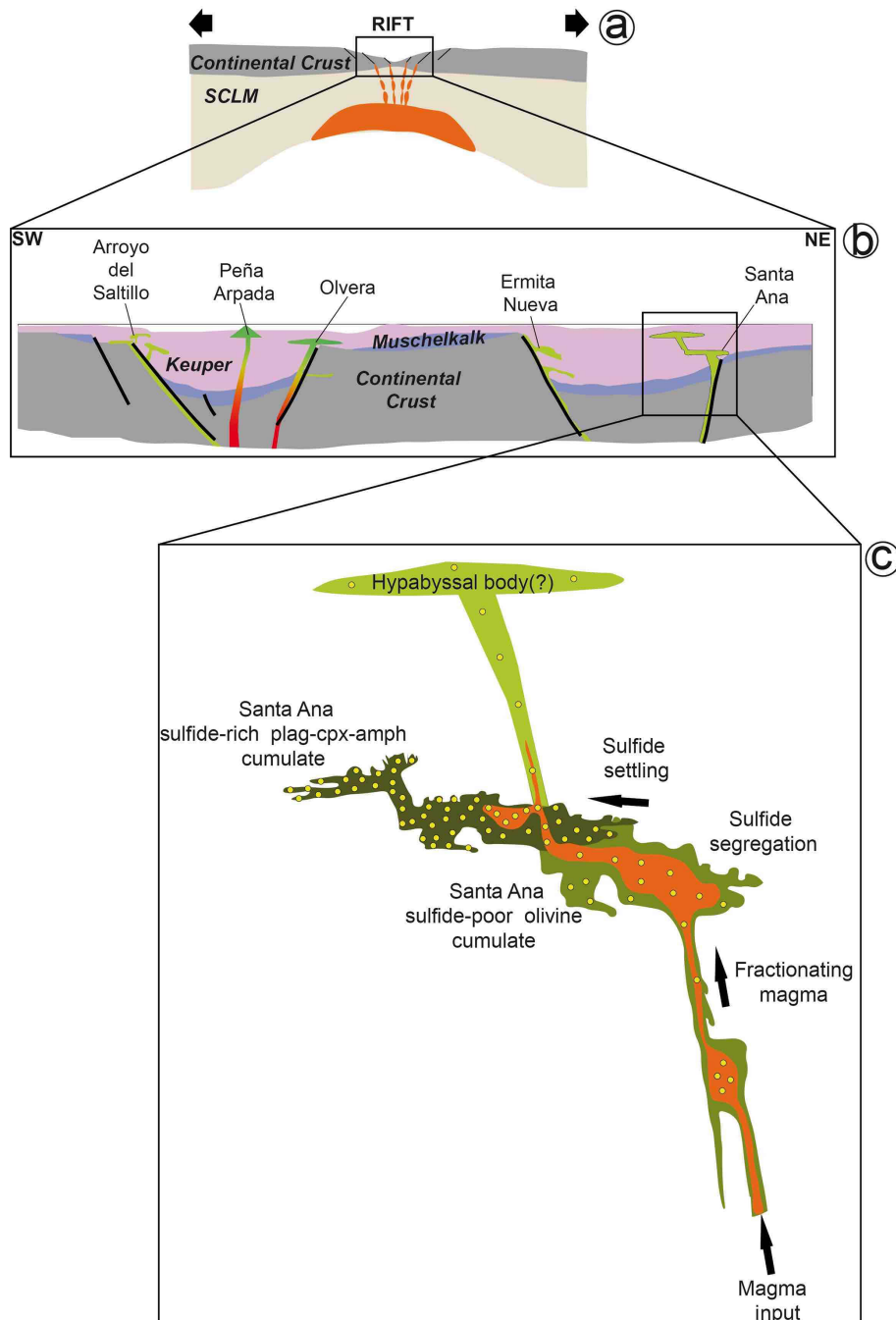


Figure 15. Genetic model for magmatic Fe–Ni–Cu sulfides in igneous basic rocks of the external zone of the Betic Cordillera. **(a)** Continental rifting aids ascent of primitive magmas derived from the subcontinental lithospheric mantle (SCLM; modified from Morata, 1993). **(b)** Structurally controlled emplacement of intraplate basaltic magmas by rifting of continental crust allows development of active (sub)volcanic plug intruding through Keuper sediments (adapted from Pérez-López et al., 2021). The ideal orientation of the dike is vertical, but it is locally reoriented into parallelism by pre-existing structures such as fractures and stratification planes. **(c)** Conduit-style injection where stagnant (conformably oriented) chambers have developed, facilitating magma-entrained primary silicate mushes being left to settle through the conduit, thus forming cumulate layers, particularly at the conduit margins, like those observed in the plutonic olivine-bearing dolerite of Santa Ana. In this case, fractional crystallization and possibly crustal contamination of the upward-moving magma promoted segregation of larger volumes of sulfide melt droplets entrained in the plug, which settled through the conduit as an interstitial or intercumulus phase along with hydrous silicates around the cumulate silicates (olivine, plagioclase and clinopyroxene). Magmas channeled upwards through the conduit interconnected with the shallower fracture network may still contain some sulfides, giving rise to hypabyssal bodies with fewer magmatic sulfides in the shallower portion of the sedimentary pile.

the Fe–Ni–S portion of the system (Fig. 16c), as the temperature drops, the metal excess in MSS is exsolved in a variety of pentlandite forms, depending on the cooling rate. Thus, at temperatures between 550–400 °C when Ni diffusion in MSS is relatively fast, pentlandite is exsolved as granular pentlandite around the margins of pyrrhotite and at the contact with chalcopyrite, where it may form loop or rim textures (Helmy et al., 2021; Smith et al., 2023). At lower temperatures, cooling rates decrease and pentlandite first exsolves as ribbons at the margin of pyrrhotite (≤ 300 °C) and as flames, fans or blades within it at ~ 100 °C (Kelly and Vaughan, 1983; Helmy et al., 2021). This crystallization evolution of sulfide melts explains our polyphase sulfide assemblages (Fig. 16) and the suite of pentlandite micro-textures well, including granular (Pn-1), granular with marginal blades (Pn-2), fans (Pn-3) and flames (Pn-4) (Figs. 6 and 7), as in experiments (e.g., Helmy et al., 2021). The lack of irregular contacts between pyrrhotite and pentlandite, at both micrometer- and nano-sized scales (Figs. 6–9 and File S5 in the Supplement), rules out the possible formation of pentlandite via peritectic reaction of MSS with coexisting Cu–Ni sulfide liquids observed in experiments (e.g., Sugaki and Kitakaze, 1998; Kitakaze et al., 2016) and nature (e.g., Mansur et al., 2019; González-Jiménez et al., 2020).

In the model proposed above, high-temperature MSS solidifies with a hexagonal lattice structure, and it breaks down into granular pentlandite with the cubic $Fm\bar{3}m$ structure below 610 °C and monoclinic pyrrhotite at 315 °C. This is consistent with the cubic $Fm\bar{3}m$ structure of granular pentlandite and the monoclinic polytype 4C of pyrrhotite identified here (Figs. 8–9, Table A1 and File S5 in the Supplement; Wang and Salveson, 2005). An exsolution-driven mechanism of Ni from pyrrhotite is further suggested by the presence of lattice fringes off cubic $Fm\bar{3}m$ pentlandite within pyrrhotite (Fig. 9; Table A1 and File S5 in the Supplement). These nanostructures are likely “relicts” of some Ni that was incompletely extracted during the diffusion processes, thus explaining the slight deviations from the ideal stoichiometry in EPMA and EDS–STEM maps of these sulfides. It is worth noting that Helmy et al. (2021) documented synthetic pyrrhotites still containing relatively high amounts of Ni (up to 7.2 wt % in the form of pentlandite nanoinclusions as observed here) in experiments equilibrated at constant temperature (15 °C d^{-1}) after 2 weeks, arguing that longer cooling times (months to years) should be necessary to account a full depletion of MSS in Ni. Therefore, the incomplete extraction of Ni in the Ni-poorer pyrrhotites analyzed in this study (< 0.43 wt %; File S4, Supplement) could reflect longer crystallization rates than in the experiments, consistent with the slow cooling rates necessary to produce ophitic and subophitic textures like those observed here (~ 7 – 10 years; Holness et al., 2015). Moreover, lattice fringes of tetragonal $I\bar{4}2d$ chalcopyrite in granular pentlandite (Pn-1) (Table A1 and File S5 in the Supplement) suggest an additional role of the Cu-rich sulfides in the formation of pentlandite. In fact, recent nanoscale ob-

servations of experimental runs by Helmy et al. (2021) have shown that a continuous “contact zone” of pentlandite may develop between MSS and ISS at 550–450 °C. Further Ni extraction from ISS within the range of 200–250 °C makes this “contact pentlandite” zone crystallize as granular pentlandite, when cooling is slowly maintained in time. This interpretation is consistent with the fact that granular pentlandite (Pn-1) is locally sandwiched between pyrrhotite and chalcopyrite and also with the slow cooling rate expected for stabilization of the disordered monoclinic structure 4C of pyrrhotite, instead of the well-ordered monoclinic 3C (Wang and Salveson, 2005).

Additionally, the identification of minute laths of chalcopyrite in fractures inside pyrrhotite (Fig. 7) suggests that significant amounts of Cu were still present in the precursor MSS after separation of the coexisting Cu–Fe–(Ni) melt. Experimental works have shown that up to 7.5 wt % Cu may be accommodated as Cu^{2+} in the hexagonal Ni–S type structure of MSS at 935 °C (Cabri, 1973; Rajamani and Prewitt, 1973; Ballhaus et al., 2001) or as exsolved nanoparticles of chalcopyrite at 950 °C (Helmy et al., 2021). We have not found discrete nanoparticles of Cu in pyrrhotite but nano-sized domains of tetragonal $I\bar{4}2d$ chalcopyrite and cubic $F\bar{4}3m$ bornite, which support an incomplete release of Cu initially bounded in the precursor MSS lattice. Thus, very low amounts of Cu and Ni (< 1 wt %) detected by EPMA suggest an almost complete sub-solidus re-equilibration of MSS into its low-temperature product pyrrhotite, very likely continuing down to low temperatures (≤ 100 °C; e.g., Kelly and Vaughan, 1983) and trapping the remaining Cu and Ni into chalcopyrite, bornite and pentlandite nanodomains (González-Jiménez et al., 2024).

On the other hand, larger chalcopyrite grains associated with both pyrrhotite and pentlandite (Figs. 6g–h and 7a–b) suggest that each volume of sulfide melt followed its own fractional crystallization path after the mechanical separation explained above. In the Fe–Cu–S portion of the system, a Ni- and Cu-rich residual sulfide melt might eventually originate after the crystallization of MSS (Fig. 16d). According to the experiments of Craig and Kullerud (1969), a Ni-poor and Cu-rich residual sulfide melt can coexist with Ni-rich MSS at ~ 900 °C, whereas at 850 °C it crystallizes into the high-temperature cubic form of chalcopyrite (i.e., ISS; Fig. 16d). Tsujimura and Kitakaze (2004) have demonstrated experimentally that at 800 °C, a Cu–Fe–S melt may exist in the S-rich portion of the Cu–Fe–S system. Upon cooling at ~ 700 °C, this sulfide melt crystallizes with a composition close to the ISS (Yund and Kullerud, 1966), which further re-equilibrates at much lower temperatures (≤ 100 °C) into chalcopyrite + pyrrhotite assemblages like those shown in Fig. 6h (Fig. 16d).

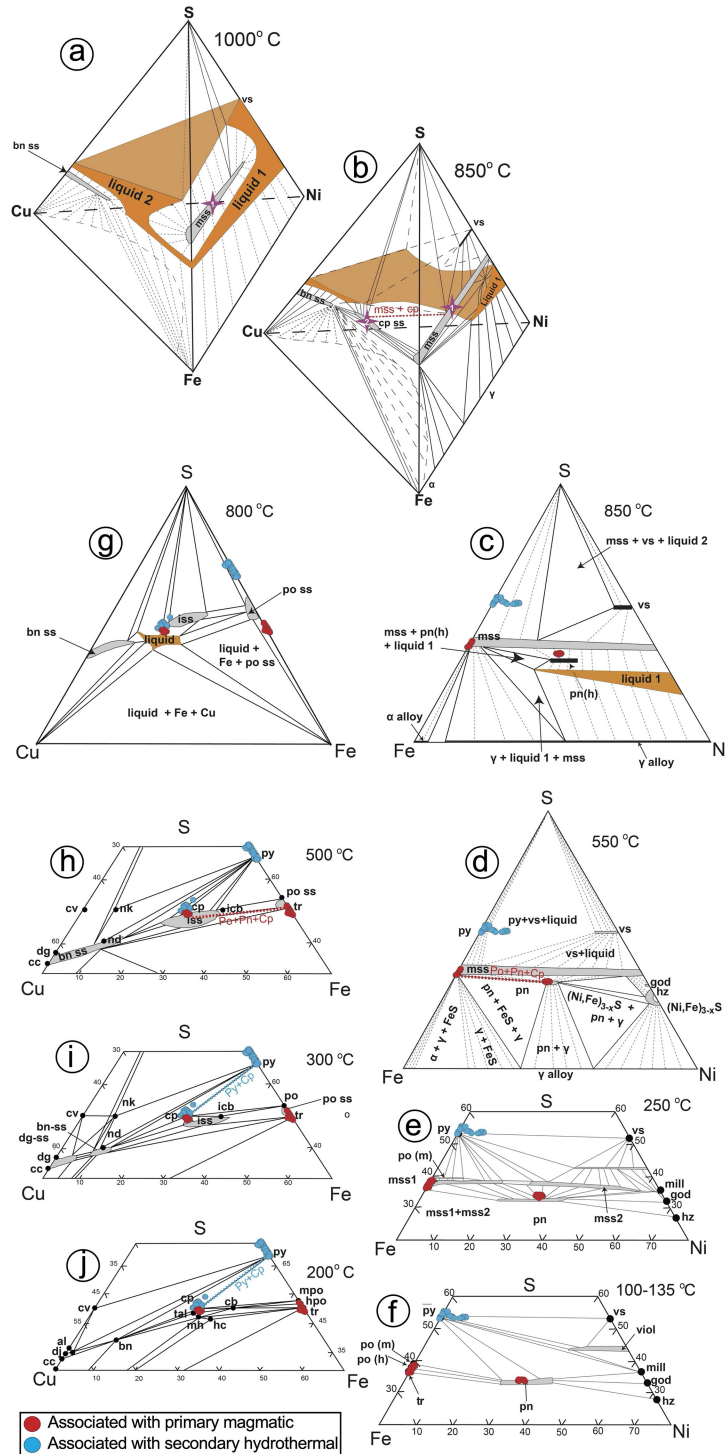


Figure 16. Phase relations (1 bar) in the sulfur-rich portion of the Cu–Fe–Ni–S system at 1000 °C (a) and 850 °C (b) with specific detail of the portions Ni–Fe–S at 850 (c), 550 (d), 250 (e) and 135–100 °C (f) and Cu–Fe–S at 800 (h), 500 (i) 300 and 200 °C (j). The figures are modified from Kullerud and Yund (1962), Craig and Kullerud (1969), Craig (1973), and Naldrett et al. (2009). Note that in (a) the MSS (purple star) coexists with two liquids at 1000 °C (a Ni–Fe-rich liquid in the Ni–Fe–S portion and a Cu-rich liquid in the Cu–Fe–S portion). At 850 °C (b), the MSS coexists with chalcopyrite (purple star), as indicated by the dotted red line. The assemblage of pyrrhotite ± pentlandite ± chalcopyrite associated with unaltered primary silicates attains equilibrium at 550–500 °C, as indicated with dotted red lines inset in (d) and (h). In contrast, the assemblage pyrite ± chalcopyrite associated with altered (secondary) silicates is stable at 300 °C and further below (i–j). Abbreviations – iss: intermediate solid solution; bn-ss: bornite solid solution; dg-ss: digenite solid solution; dg: digenite (Cu₉S₅); cv: covellite (CuS); cc: chalcocite (Cu₂S); icb: isocubanite (CuFe₂S₃); hc: haycockite (Cu₄Fe₅S₈); nk: nukundamite (Cu₅FeS₆); nd: idaite (Cu_{5+x}FeS_{6+x}); mh: mooihoeite (Cu₉Fe₉S₁₆); tal: talnakhite (Cu₉Fe₈S₁₆); al: anilite (Cu₇S₄); dj: djurleite (Cu₃₁S₁₆); mss: monosulfide solid solution [(Fe,Ni)_{1±x}S]; vs: vaesite (NiS₂); po (m): monoclinic pyrrhotite (Fe_{1±x}S); po (h): hexagonal pyrrhotite (Fe_{1±x}S); tr: troilite (FeS); py: pyrite (FeS₂); pn: pentlandite [(Ni,Fe)₃S₈]; viol: violarite (FeNi₃S₄); mill: millerite (NiS); god: godlevskite (Ni₇S₆); hz: heazlewoodite (Ni₃S₂).

6.3 Possible segregation of Ni-poor, Cu–Fe–S-rich sulfide melt in the olivine-free hypabyssal dolerites

Some pyrite ± chalcopyrite grains identified in the olivine-free hypabyssal dolerites are fully hosted within (e.g., Fig. 10b) or are intergranular between (e.g., Fig. 10e–f) partially altered magmatic clinopyroxene and/or plagioclase. The bleb-like morphology of these sulfides raises the question of whether they are solid products of sulfide melts which were segregated contemporaneously with or shortly after the igneous silicates prior to hydrothermal alteration.

Clinopyroxene in dolerites from Alcalá de los Gazules and Arroyo del Saltillo is Ti, Na- and Al-poor augite (Fig. 5a–b, Supplement) with lower trace element abundances, no Eu fractionation and less negative Pb anomalies than diopside in the Santa Ana stock (Fig. 5c). These features support the claim that clinopyroxene crystallized from subalkaline tholeiitic magmas (Portugal-Ferreira et al., 1995; Morata et al., 1997) after precipitation of plagioclase from melts less differentiated than in the Santa Ana stock. Moreover, lower trace element contents and MREE / HREE fractionations in clinopyroxene (Fig. 5c) support the notion that subalkaline tholeiitic melts were derived by higher degrees of melting of a shallower lithospheric mantle source compared to the transitional-alkaline melts of Santa Ana, likely during more mature stages of continental rifting (Pérez-López et al., 2021). The calculated compositions of melts in equilibrium with clinopyroxene of dolerites from Alcalá de los Gazules and Arroyo del Saltillo, using a set of partition coefficients consistent with its augitic composition and the tholeiitic affinity of parental melts, are similar to those of the Santa Ana stock (Fig. 5d). This calculation reproduces the large overlap in terms of REE between transitional-alkaline and tholeiitic magmatism in the external zone of the Betic Cordillera well (Morata et al., 1997; Groups 2 and 3 of Pérez-López et al., 2021). This would suggest that parental magmas of these dolerites (and by extension those of the geochemically similar dolerites from Ermita Nueva and Peña Arpada) could a priori saturate sulfides by processes similar to the parental melts of the Santa Ana cumulitic stock. However, experimental work shows that pyrite does not form on the solidus of conventional basaltic melt (Kullerud and Yoder, 1959) but via (1) exsolution from S-rich MSS on cooling (e.g., Naldrett et al., 1967; Piña et al., 2013) or (2) Fe loss in Fe-rich MSS during post-cumulus re-equilibration (e.g., González-Jiménez et al., 2018) with an important role of late magmatic hydrothermal fluids (Djon and Barnes, 2012; Piña et al., 2013). This is consistent with nanodomains of pyrrhotite with the disordered monoclinic structure 4C ($\text{Fe}_{0.875}\text{S}$ or Fe_7S_8) found within pyrite (e.g., Fig. 13c). These nanodomains may be the low-temperature product of re-equilibration of high-temperature magmatic MSS with the close-packed hexagonal (NiAs) structure or its low-temperature derivate pyrrhotite 11H ($\text{Fe}_{10}\text{S}_{11}$) (Wang and Salveson, 2005). In fact, pyrite analyzed here hosts ap-

preciable quantities of metals that are compatible in MSS (i.e., Ni, Co and Cu).

The exsolution of pyrite from MSS rich in S takes place at temperatures below 700 °C (Naldrett and Kullerud, 1967; Naldrett et al., 1967). This exsolution requires the immiscible segregation of a Ni-poor, Cu–Fe–S-rich sulfide melt, which is very unlikely to occur from magmas subsaturated in olivine (Korneeva et al., 2020). In the model proposed above, such types of sulfide melts could be originated if Fe- and Ni-rich sulfides first segregated in a deep magmatic chamber, leaving behind Ni-poor, Cu-rich sulfide melts that eventually crystallized along with pyroxene and plagioclase in the shallower hypabyssal domains (McDonald and Holwell, 2007; McDonald et al., 2009; Ihlenfeld and Keays, 2011). However, this deep “plutonic” portion of a connected plumbing system is absent near the olivine-free hypabyssal dolerites from the external Betics.

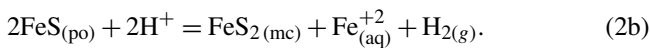
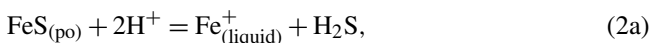
The second possibility for the formation of magmatic-related pyrite is that precursor Fe-rich MSS underwent significant chemical readjustment through a different fractional pathway. In this scenario, original Fe-rich MSS could be depleted in iron before or once it was sealed in primary silicates as result of the preferential partitioning of Fe^{2+} into coexisting pyroxene or Fe-oxides (e.g., ilmenite). Therefore, the composition of the MSS would be shifted towards Fe-poorer and S-richer composition (Naldrett et al., 1989, 2009), giving rise, in an extreme case, to a nearly stoichiometric FeS_2 . A similar mechanism would have produced Fe loss in the ISS, shifting its composition towards the Cu–S joint of the Cu–Fe–S system. Phase relations within the ternary Cu–Fe–S system predict that pyrite can coexist in equilibrium with ISS at ~ 700 °C, and further re-equilibration of ISS at lower temperature may produce pyrite + chalcopyrite assemblages similar to those in dolerites from the external Betics (Fig. 16d).

6.4 Metamorphic-related hydrothermal pyrite in the olivine-free hypabyssal dolerites

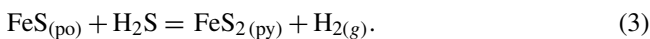
Most pyrite (± chalcopyrite) grains in the olivine-free hypabyssal dolerites are intimately intergrown with metamorphic silicates (chlorite, epidote, saussurite, prehnite, sericite and quartz; Figs. 12–13). Such a textural relationship links those sulfides with the hydrothermal alteration processes experienced by dolerites during metamorphism. In these rocks, chlorite and amphibole are the dominant alteration phases, bracketing hydrothermal alteration within the sub-greenschist to greenschist facies metamorphism at ~ 221 – 278 °C (File S2, Supplement). This range of temperature is consistent with the presence in pyrite of nanodomains of marcasite, which may form along with pyrite as a thermodynamically metastable phase via hydrothermal Fe loss or S addition in pyrrhotite at < 300 °C under varying conditions of pH, E_h , $f\text{O}_2$ and $f\text{S}_2$ (Wang et al., 2006; Qian et al., 2011; Yao et al., 2020, 2021). This is consistent with

the presence of relict pyrrhotite-4C in pyrite too, which is only stable above 326 °C (Wang et al., 2006; Yao et al., 2020, 2021, and references therein). This nanoscale observation is twofold: (1) it suggests an almost complete transformation of the parental pyrrhotite by interaction with hydrothermal fluid and (2) it indicates that once pyrite and/or marcasite formed through nanoscale conversion of precursor pyrrhotite, they could grow to macroscopic crystals from supersaturated solutions. Qian et al. (2011) showed that transformation of pyrrhotite to pyrite and/or marcasite at the nanometer scale is strongly controlled by pH and the saturation index rather than by E_h , fO_2 and fS_2 of the fluid. Thus, the latter authors documented pyrite formation by direct replacement of pyrrhotite and, simultaneously, by overgrowth from solution if $pH > 5$ and saturation indices are > 1000 . In contrast, formation of marcasite is favored at $pH < 4$ if the solution is (S^{-2})-deficient with a saturation index $\ll 1000$. The predominance of pyrite over marcasite in our samples does not necessarily indicate high pH but may instead reflect the aforementioned (S^{-2})-rich nature of the hydrothermal fluid, which may have favored pyrite formation after pyrrhotite via S addition instead of Fe loss.

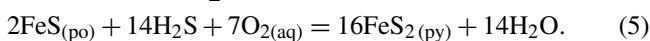
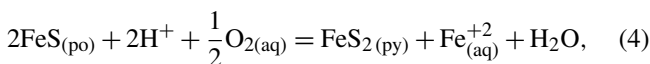
However, the latter mechanism does not rule out marcasite as a possible intermediate product, at least at the earliest stages of alteration (e.g., Xia et al., 2009a; Qian et al., 2011). Marcasite may have formed via a Fe-loss pathway according to the following reaction (Benning et al., 2000; Butler et al., 2004; Qian et al., 2011):



As the reaction progressed, pyrite may have formed via S addition during reaction of pyrrhotite with H_2S (Eq. 2a) (Rickard and Luther, 2007) as follows:



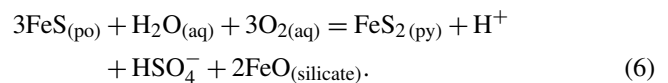
The Fe-loss and S-addition pathways usually take place under anaerobic conditions and produce $H_{2(g)}$ (i.e., H^+ is the oxidant). However, some authors (e.g., Murowchick, 1992; Qian et al., 2011) have suggested an alternative “ O_2 pathway” (i.e., oxidic and acidic) to emphasize the need for an external oxidant, proposing the following reactions:



Experimental syntheses (Qian et al., 2011; Yao et al., 2020, 2021) show that both anaerobic and oxic mechanisms are viable, although the oxic route is the most thermodynamically and kinetically favorable. The key observation extracted from the aforementioned experiments is that reactions producing mainly marcasite are usually conservative with respect to S (pathways of Fe loss in Eqs. 2a and 2b and O_2 in Eq. 4),

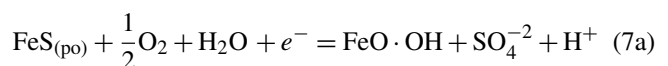
whereas those producing mainly pyrite tend to conserve Fe (O_2 and H_2S pathways; Eqs. 3 and 5). All these reactions produce a strong volume decrease and micrometer-sized porosity in the resulting iron disulfide, a feature observed in the pyrite analyzed here (Fig. 10).

Phase relations between pyrrhotite and pyrite in hydrothermal experiments show that formation of pyrite after pyrrhotite requires increasingly higher fugacity of H_2S and O_2 in the fluid (Kusebauch et al., 2018). Under the conditions of greenschist facies metamorphism, the hydration of igneous silicates to form secondary chlorite, epidote and amphibole decreases H_2O and increases fS_2 and fO_2 in the system (e.g., Kanitpanyacharoen and Boudreau, 2012). This effect could drive the stabilization of pyrite over pyrrhotite and marcasite in the fS_2 - fO_2 - T thermochemical space. The observation that alteration haloes of some silicates occur about sulfide (Figs. 10 and 11) suggests that the presence of sulfide enhanced the formation of the greenschist silicate assemblage by the following reaction:

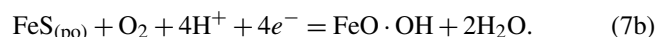


The H^+ ions produced in this reaction, Eq. (6), may have been incorporated into hydrous alteration minerals, thus producing more pyrite with increasing alteration in surrounding silicates.

Additionally, the identification of goethite at the contacts between pyrite and secondary quartz confirms the oxic route in our case study. It further denotes that sufficient O_2 was left after Eqs. (4), (5) and (6) to eventually react with Fe_{aq}^{2+} released by the dissolution of pyrrhotite (Eq. 4) to form this oxide. The electrochemically coupled reaction of goethite formation took place preferentially on the pyrrhotite surface and can be expressed as follows (Waal, 1984):



or



The path shown in Eqs. (7a) and (7b) implies loss of S during open-system reactions and drives pyrrhotite transformation to goethite, avoiding intersection with the pyrite stability field, likely postdating pyrite formation.

On the other hand, pyrite + quartz infilling veins crosscutting the metamorphic minerals at Ermita Nueva (Fig. 10h) suggest direct precipitation from late-stage metamorphic hydrothermal fluids (Pokrovski et al., 2021). In this body, the metamorphic assemblage is dominated by chlorite \pm epidote \pm albite \pm calcite \pm quartz, suggesting a metamorphic reaction at ~ 237 – 251 °C (File S2, Supplement). Preferential alteration of both clinopyroxene and plagioclase likely led to high silica activity in solution, thus promoting deposition of pyrite along with the late-stage quartz (Alt et

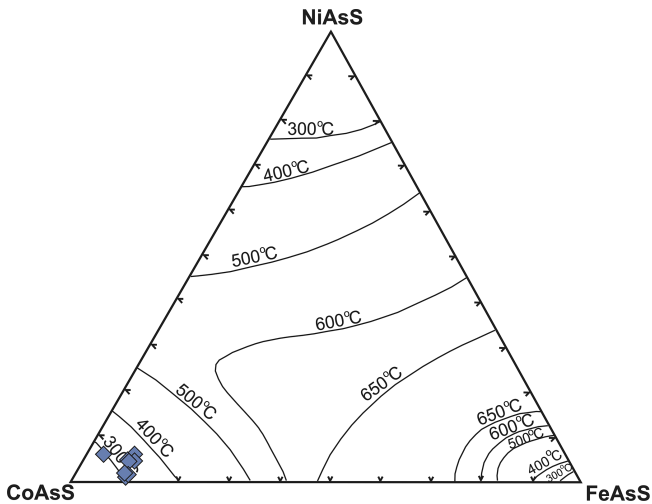
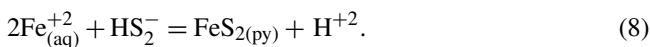


Figure 17. Plot of the analyzed cobaltite rim with references of the solvus in the condensed system CoAsS–NiAsS–FeAsS at 300, 400, 500, 600 and 650 °C (Klemm, 1965). Note that the temperature of equilibration of cobaltite overlaps that of metamorphism-related hydrothermal alteration of the host rock.

al., 2007; Ray et al., 2009). Experimental works suggest that homogenous nucleation of pyrite is insignificant in acidic and slightly acidic solutions under < 300 °C (because it requires an extremely high saturation index of 5.7×10^{14} ; Rickard and Luther, 1997). Nonetheless, more recent works demonstrate that high saturation may be overcome by non-conventional crystal growth via stabilization and coalescence of nanoparticulate pyrite in the hydrothermal fluid (Yücel et al., 2011; Gartman et al., 2014; Findlay et al., 2019). This mechanism experimentally tested at both micrometer (Rickard and Luther, 2007) and nanometer scales (Yao et al., 2021) can be expressed as follows:

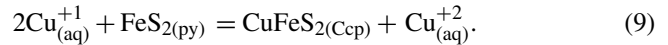


The constituents Fe^{2+} and H_2S or HS^- are usually dissolved in the aqueous silica-rich fluid produced during the latest stages of hydrothermal alteration of gabbroic rocks in seafloor basins (e.g., Alt and Shanks, 1998).

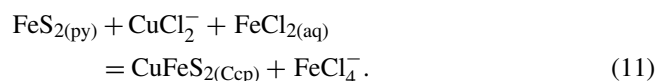
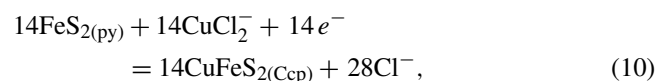
6.5 Replacive rims of Fe–Cu sulfides and Co–Ni sulfarsenides in pyrite

Pyrite from olivine-free hypabyssal rocks exhibits rims of chalcopyrite or cobaltite, as well as pores infilled by nanometer- to micrometer-sized inclusions of chalcopyrite-preserving domains of pyrite, pyrrhotite and vaesite (Fig. 10c–g and File S6 in the Supplement). Rickard and Cowper (1994) experimentally tested the direct replacement of pyrite to chalcopyrite by reaction of pyrite with aqueous $\text{Cu}_{(\text{aq})}^{+2}$ at < 200 °C and pH = 3.0–4.5. In these experiments, chalcopyrite was an intermediate product that is ultimately transformed to bornite and digenite in the presence

of excess aqueous Cu^{+2} . However, Cu^{+1} is a more common species in the redox state, prevailing in fluids involved in the hydrothermal alteration of gabbroic rocks. According to Rickard and Cowper (1994), pyrite may react with aqueous Cu^{+1} at 100 °C, giving rise to chalcopyrite through the following reaction:



However, more recent studies have shown that in hydrothermal fluids, Cu^{+1} is preferentially transported as hydrosulfide ($\text{Cu}(\text{HS})_2^-$; Mountain and Seward, 2003) and chloride (CuCl , CuCl_2^- , CuCl_3^{2-} ; Etschmann et al., 2010) complexes. To date, experimental investigation of pyrite replacement by chalcopyrite via interaction with hydrothermal fluids is only available for Cu-rich chloride complexes (Zhang et al., 2021). The results of these experiments carried out at 100–250 °C showed that chalcopyrite forms after pyrite if the fluid is acidic to neutral (pH = 3.0–6.0) at > 150 °C. They also showed that this is a redox-coupled dissolution–precipitation reaction, with the oxidative dissolution of pyrite to form sulfate, generating the electrons that maintain the reductive replacement of pyrite by chalcopyrite. In our case study, direct overgrowth of chalcopyrite around porous pyrite grains highlights the role that the network of micrometer-size pores played to enable the chemical exchanges between pyrite and the fluid (see the islands of pyrite within chalcopyrite following pre-existing pores in Fig. 10e–g). Zhang et al. (2021) have also observed such a replacement mechanism in their experiments, proposing a redox-coupled dissolution–precipitation reaction in chloride-rich hydrothermal fluids as follows:



It is worth noting that we have also identified relicts of pyrrhotite within chalcopyrite at both micrometer (Fig. 11f) and nanometer (Fig. 14c) scales, thus providing additional evidence for the replacive origin of chalcopyrite. The experimental work by Cooper and Rickard (1989) supports the notion that chalcopyrite may form via reaction of pyrrhotite with Cu^{+2} in sulfate solutions at < 100 °C. Therefore, the coexistence within chalcopyrite of both pyrrhotite and pyrite nanodomains suggests two alternative pathways for its formation of this Cu-rich sulfide in our samples: (1) pyrrhotite → pyrite/marcasite → chalcopyrite and (2) pyrrhotite → chalcopyrite. In this model, nano- to micrometer-sized inclusions of chalcopyrite in pores of pyrite after pyrrhotite and of vaesite (NiS_2), sphalerite (ZnS) and galena (PbS) within replacive rims of chalcopyrite could correspond to metals initially contained in pyrite (or pyrrhotite) precursor, which were re-precipitated in situ at the

mineral interface of the pores. As noted above, many pyrite grains analyzed here contain Cu, Ni, Zn and Pb in amounts detectable by EPMA, which may have been liberated from the pyrite structure during replacement reactions (e.g., Deditius et al., 2011; Yao et al., 2020) and stabilized during low-temperature alteration at < 200 °C.

The microstructural position of cobaltite at the margins of pyrite in Saltillo dolerites (Fig. 11g–h) suggests its latter formation relative to the sulfide. A formation temperature of ~ 300 °C is suggested for this cobaltite based on its low nickel and Fe contents (Fig. 17), consistent with temperatures of metamorphism recorded in the host rock.

7 Conclusions

Plutonic and hypabyssal basic rocks intruding the Triassic sediments of the external zone of the Betic Cordillera in southern Spain host assemblages of magmatic and hydrothermal Fe–Ni–Cu (pyrrhotite, pentlandite, chalcopyrite, pyrite, marcasite and vaesite), and Fe–Zn–Pb sulfides (sphalerite and galena). Magmatic Fe–Ni–Cu sulfides crystallized from sulfide melts segregated by immiscibility from intraplate basaltic melts injected through magma conduits in the breaking up of continental crust during the initial stages of continental rifting. Nanoscale observations allow disclosing the solidification of Fe–Ni–S melt into MSS and a remaining Cu–Fe–S melt into ISS, which later re-equilibrated at low temperature into pyrrhotite \pm pentlandite \pm chalcopyrite assemblages. In contrast, pyrite \pm chalcopyrite grains associated with metamorphic silicates (chlorite, epidote, saussurite, prehnite, sericite and quartz) are linked to metamorphic-related hydrothermal alteration of the dolerite. The nanoscale study suggests that hydrothermal pyrite (\pm marcasite) formed via replacement of pre-existing Fe-rich MSS at < 300 °C. In contrast, hydrothermal chalcopyrite could form according to the two following alternative pathways: (1) pyrrhotite \rightarrow pyrite/marcasite \rightarrow chalcopyrite or (2) pyrrhotite \rightarrow chalcopyrite. Additionally, remobilization of Zn, Pb, Ni and Co during hydrothermal alteration is supported by minute inclusions of sphalerite, galena and vaesite in secondary pyrite (and chalcopyrite) as well as rims of cobaltite around them.

Appendix A

Table A1. Summary of characteristic indexed FFT d -spacing values for the unaltered sulfide from Santa Ana shown in Figs. 8 and 9. Data source for reference d spacings: monoclinic $C2/c$ polytype 4C pyrrhotite (Powell et al., 2004); cubic $Fm\bar{3}m$ pentlandite (Tsukimura et al., 1992; Tenaillé et al., 2006); tetragonal $I4\bar{2}d$ chalcopyrite (Knight et al., 2011); cubic $F\bar{4}3m$ bornite (Ding et al., 2005a, b).

Measured d spacing (Å)	Pyrrhotite (monoclinic $C2/c$ polytype 4C)	Pentlandite (cubic $Fm\bar{3}m$)	Chalcopyrite (tetragonal $I4\bar{2}d$)	Bornite (cubic $F\bar{4}3m$)
12.313–11.714	12.895–11.865 Å {001}			
6.112–5.691		5.891–5.853 Å (111)		
5.308–5.300	5.305 Å ($\bar{2}02$)			
4.847		5.102 Å (200)		
4.808–4.613	4.702–4.589 Å ($\bar{1}12$)			
3.652–3.547		3.607–3.584 Å (220)		
3.128	3.133 Å ($\bar{3}13$)			
3.085–3.045		3.076–3.057 Å for (311)		
3.083	3.109 Å (310)			
3.046–3.028			3.038 Å (112)	
2.993–2.924		2.9458–2.926 Å (222)		
2.407–2.376	2.376–2.370 Å ($\bar{3}15$)			
2.365–2.360	2.3457 Å (312)	2.3411 Å (314)		
2.348	2.3457 Å (312)			
2.203–2.185	2.207–2.195 Å ($\bar{4}21$)			
2.128–2.095	2.124 Å (204)			
2.099–2.060		2.083–2.069 Å (442)		
2.024–2.018		2.021–2.012 Å ($\bar{1}33$)		
1.997–1.948		1.963–1.951 Å (333)		
1.852–1.833			1.836–1.856 Å (204)	
1.832–1.778		1.803–1.792 Å (440)		
1.316–1.308				1.337 Å (800)
1.356–1.309			1.302 Å (008)	

Data availability. All data derived from this research are original data obtained by the authors for the present study and are presented in the enclosed tables, figures and Supplement.

Supplement. The supplement related to this article is available online at <https://doi.org/10.5194/ejm-37-191-2025-supplement>.

Author contributions. All authors contributed to the study conception and design. Fieldwork in the Betic Cordillera (Spain) was carried out by JMGJ, IFBQ, CM, FAJC, LY and FG. Material preparation, data collection and analysis were performed by JMGJ, IGP, ARFG and LY. The first draft of the manuscript was written by JMGJ and ES, and all authors commented on previous versions of the manuscript. All authors read and approved the final manuscript.

Competing interests. The contact author has declared that none of the authors has any competing interests.

Disclaimer. Publisher's note: Copernicus Publications remains neutral with regard to jurisdictional claims made in the text, published maps, institutional affiliations, or any other geographical representation in this paper. While Copernicus Publications makes every effort to include appropriate place names, the final responsibility lies with the authors.

Acknowledgements. We wish to acknowledge the assistance of Jesús Montes (Department of Mineralogy and Petrology, Universidad de Granada) in the preparation of the polished sections and the assistance of Cristobal Cantero (Servicios Centrales de Investigación of the Universidad de Huelva) and Isabel Sánchez Almazo (Centro de Instrumentación Científica of the Universidad de Granada) and Manuel Jesús Román Alpiste (IACT-CSIC) for their assistance with EPMA, FE-SEM and LA-ICP-MS respectively. Authors also acknowledge the use of instrumentation as well as the technical advice provided by the national facility ELECOM ICTS node "Laboratorio de Microscopías Avanzadas" at the Universidad de Zaragoza. We would like to thank Laura Casado Zueras, Alfonso Ibarra, and Rodrigo Fernández-Pacheco Chicón from LMA (Laboratorio de Microscopías Avanzadas) of the Universidad de Zaragoza, as well as José María Geraldía Sánchez and Lorena González Souto, for their invaluable help with the FIB and HRTEM sample preparation and analyses. José Juan Calvino Gámez from the Universidad de Cádiz is also acknowledged for his input to TEM data interpretation. The authors are also grateful to José María González Benítez and Josefa Jiménez García for their help and attention during fieldwork in the area.

Financial support. This research has been supported by the project PROYEXCEL_00705 "Metallogeny of Cobalt in the Betic Cordillera" (grant no. P21-00705), funded by the Consejería de Transformación Económica, Industria, Conocimiento y Universidades de la Junta de Andalucía.

The article processing charges for this open-access publication were covered by the CSIC Open Access Publication Support Initiative through its Unit of Information Resources for Research (URICI).

Review statement. This paper was edited by Riccardo Tribuzio and reviewed by Maria Rosaria Renna, Hassan Helmy, and one anonymous referee.

References

- Alt, J. C. and Shanks, W. C.: Sulfur in serpentinized oceanic peridotites: serpentinization processes and microbial sulfate reduction, *J. Geophys. Res.*, 103, 9917–9929, <https://doi.org/10.1016/j.gca.2021.04.017>, 1998.
- Alt, J. C., Shanks, W. C., Bach, W., Paulick, H., Garrido, C. J., and Baudoin, G.: Hydrothermal alteration and microbial sulfate reduction in peridotite and gabbro exposed by detachment faulting at the Mid-Atlantic Ridge, 15°20' N (ODP Leg 209): a sulfur and oxygen isotope study, *Geochem. Geophys. Geosys.*, 8, Q08002, <https://doi.org/10.1029/2007GC001617>, 2007.
- Ballhaus, C., Tredoux, M., and Spaeth, A.: Phase relations in the Fe-Ni-Cu-PGE-S system at magmatic temperature and application to massive sulfide ores of the Sudbury Igneous Complex, *J. Petrol.*, 42, 1911–1926, <https://doi.org/10.1093/petrology/42.10.1911>, 2001.
- Benning, L. G., Wilkin, R. T., and Barnes, H. L.: Reaction pathways in the Fe–S system below 100 °C, *Chem. Geol.*, 167, 25–51, [https://doi.org/10.1016/S0009-2541\(99\)00198-9](https://doi.org/10.1016/S0009-2541(99)00198-9), 2000.
- Blanco-Quintero, I. F., Martín-Algarra, A., Santamaría-Pérez, E., González-Jiménez, J. M., Navas, A. S., Benavente, D., Cañaveras, J. C., and García-Casco, A.: Barrovian metamorphism in nominally lowermost Alpujarride Complex units: tectonic implications for the development of the orogenic wedge in the Western Mediterranean, *Int. Geol. Rev.*, 66, 439–462, <https://doi.org/10.1080/00206814.2023.2233102>, 2024.
- Blanks, D. E., Holwell, D. A., Fiorentini, M. L., Moroni, M., Giuliani, A., Tassara, S., González-Jiménez, J. M., and Boyce, A. J., Ferrari, E.: Fluxing of mantle carbon as a physical agent for metallogenic fertilization of the crust, *Nat. Commun.*, 11, 1–11, <https://doi.org/10.1038/s41467-020-18157-6>, 2020.
- Bonechi, B., Perinelli, C., Petrelli, M., Gaeta, M., Fabbriozio, A., and Strnad, L.: High pressure trace element partitioning between clinopyroxene and alkali basaltic melts, *Geochim. Cosmochim. Acta.*, 305, 282–305, <https://doi.org/10.1016/j.gca.2021.04.023>, 2021.
- Butler, I. B., Böttcher, M. E., Rickard, D., and Oldroyd, A.: Sulfur isotope partitioning during experimental formation of pyrite via the polysulfide and hydrogen sulfide pathway: implications for the interpretation of sedimentary and hydrothermal pyrite isotope records, *Earth Planet. Sc. Lett.*, 228, 495–509, <https://doi.org/10.1016/j.epsl.2004.10.005>, 2004.
- Cabri, L. J.: New data on phase relations in the Cu-Fe-S system, *Econ. Geol.*, 64, 443–454, <https://doi.org/10.2113/gsecongeo.68.4.443>, 1973.

- Cooper, M. M. and Rickard, D.: Mechanism of chalcopyrite formation from iron monosulfides in aqueous solutions (<100 °C, pH 2–4.5), *Chem. Geol.*, 78, 325–342, [https://doi.org/10.1016/0009-2541\(89\)90067-3](https://doi.org/10.1016/0009-2541(89)90067-3), 1989.
- Craig, J. R.: Pyrite-pentlandite assemblages and other low temperature relations in the Fe-Ni-S system, *Am. J. Sci.*, 273, 496–510, 1973.
- Craig, J. R. and Kullerud, G.: Phase relations in the Cu-Fe-Ni-S system and their application to magmatic ore deposits, *Econ. Geol. Monogr.*, 4, 344–358, <https://doi.org/10.5382/Mono.04.25>, 1969.
- Cox, K. G., Bell, J. D., and Pankhurst, R. J. (Eds.): *The interpretation of the igneous rocks*, Allen & Unwin, London, 450 pp., 1979.
- Deditius, A. P., Utsunomiya, S., Reich, M., Kesler, S. E., Ewing, R. C., Hough, R. M., and Walshe, J. L.: Trace metal nanoparticles in pyrite, *Ore Geol. Rev.*, 42, 32–46, <https://doi.org/10.1016/j.oregeorev.2011.03.003>, 2011.
- Desmurs, L., Müntener, O., and Manatschal, G.: Onset of magmatic accretion within a magma-poor rifted margin: a case study from the Platta ocean-continent transition, eastern Switzerland, *Contrib. Mineral. Petrol.*, 144, 365–382, <https://doi.org/10.1007/s00410-002-0403-4>, 2002.
- De Villiers, J. P. R., Liles, D. C., and Becker, M.: The crystal structure of a naturally occurring 5C pyrrhotite from Sudbury, its chemistry, and vacancy distribution, *Am. Mineral.*, 94, 1405–1410, <https://doi.org/10.2138/am.2009.3081>, 2009.
- Díaz de Neira Sánchez, J. A., Enrile-Albir, A., Hernaiz-Huertas, P. P., and López-Olmedo, F.: Hoja Alcalá la Real (no. 990), Mapa Geológico de España 1 : 50 000, Segunda serie, I.G.M.E., Madrid, ISBN: 84-7840-112-1, 1988.
- Ding, Y., Veblen, D. R., and Prewitt, C. T.: High-resolution transmission electron microscopy (HRTEM) study of the 4a and 6a superstructure of bornite Cu_5FeS_4 , *Am. Mineral.*, 90, 1256–1262, <https://doi.org/10.2138/am.2005.1517>, 2005a.
- Ding, Y., Veblen, D. R., and Prewitt, C. T.: Possible Fe / Cu ordering schemes in the 2a superstructure of bornite (Cu_5FeS_4), *Am. Mineral.*, 90, 1265–1269, <https://doi.org/10.2138/am.2005.1518>, 2005b.
- Djon, M. L. N. and Barnes, S. J.: Changes in sulfides and platinum-group minerals with the degree of alteration in the Roby, Twilight, and High-Grade Zones of the Lac des Iles Complex, Ontario, Canada, *Mineral Depos.*, 47, 875–896, <https://doi.org/10.1007/s00126-012-0401-z>, 2012.
- Durand, C. J., Barnes, S. J., and Corkery, J. T.: Geology, petrography, geochemistry, and genesis of sulfide-rich pods in the Lac des Iles palladium deposits, western Ontario, Canada, *Mineral Depos.*, 51, 509–532, <https://doi.org/10.1007/s00126-015-0622-z>, 2016.
- Etschmann, B. E., Liu, W., Testemale, D., Müller, H., Rae, N. A., and Proux, O.: An in situ XAS study of copper(I) transport as hydrosulfide complexes in hydrothermal solutions (25–592 °C, 180–600 bar): Speciation and solubility in vapor and liquid phases, *Geochim. Cosmochim. Acta*, 74, 4723–4739, <https://doi.org/10.1016/j.gca.2010.05.013>, 2010.
- Farmer, G. L.: Continental Basaltic Rocks, in: *Treatise on Geochemistry*, Vol. 3, The Crust, edited by: Holland, H. D., Turekian, K. K., Elsevier, 85–121, <https://doi.org/10.1016/B0-08-043751-6/03019-X>, 2003.
- Fleet, M. E. and Pan, Y.: Fractional crystallization of anhydrous sulfide liquid in the system Fe-Ni-Cu-S, with application to magmatic sulfide deposits, *Geochim. Cosmochim. Acta*, 58, 3369–3377, [https://doi.org/10.1016/0016-7037\(94\)90092-2](https://doi.org/10.1016/0016-7037(94)90092-2), 1994.
- Ferrario, A. and Garuti, G.: Platinum-group mineral inclusions in chromitites of the Finero mafic-ultramafic complex (Ivrea-Zone, Italy), *Mineral. Petrol.*, 41, 125–143, <https://doi.org/10.1007/BF01168491>, 1990.
- Findlay, A. J., Estes, E. R., Gartman, A., Yücel, M., Kamysny, A., and Luther III, G. W.: Iron and sulfide nanoparticle formation and transport in nascent hydrothermal vent plumes, *Nat. Commun.*, 10, 1597, <https://doi.org/10.1038/s41467-019-09580-5>, 2019.
- García de Domingo, A., González-Lasta, J., Hernaiz-Huertas, P. P., Zazo-Cardeña, C., and Goy-Goy, J. L.: Hoja Chiclana de la Frontera (no. 1069), Mapa Geológico de España E 1 : 50 000, Segunda serie, I.G.M.E., Madrid, M-10374-1991, 1983.
- Gartman, A., Findlay, A. J., and Luther III, G. W.: Nanoparticulate pyrite and other nanoparticles are a widespread component of hydrothermal vent black smoker emissions, *Chem. Geol.*, 366, 32–41, <https://doi.org/10.1016/j.chemgeo.2013.12.013>, 2014.
- González-Jiménez, J. M., Deditius, A., Gervilla, F., Reich, M., Suvorova, A., Roberts, M. P., Roqué, J., and Proenza, J. A.: Nanoscale partitioning of Ru, Ir, and Pt in base-metal sulfides from the Caridad chromite deposit, Cuba, *Am. Mineral.*, 103, 1208–1220, <https://doi.org/10.2138/am-2018-6424>, 2018.
- González-Jiménez, J. M., Proenza, J. A., Pastor-Oliete, M., Saunders, E., Aiglsperger, T., Pujol-Solà, N., Melgarejo, J. C., Gervilla, F., and García-Casco: Precious metals in magmatic Fe-Ni-Cu sulfides from the Potosí chromite deposit, eastern Cuba, *Ore Geol. Rev.*, 118, 103339, <https://doi.org/10.1016/j.oregeorev.2020.103339>, 2020.
- González-Jiménez, J. M., González-Pérez, I., Plissart, G., Ferreira, A. R., Schettino, E., Yesares, L., Schilling, M. E., Corgne, A., and Gervilla, F.: Micron-to-nanoscale investigation of Cu-Fe-Ni sulfide inclusions within laurite (Ru, Os) S_2 from chromitites, *Mineral Depos.*, 60, 581–604, <https://doi.org/10.1007/s00126-024-01285-0>, 2024.
- Gualtieri, A. and Venturelli, P.: In situ study of the goethite-hematite transformation by real time synchrotron powder diffraction, *Am. Mineral.*, 84, 895–904, <https://doi.org/10.2138/am-1999-5-625>, 1999.
- Guerrera, F., Martín-Martín, M., and Tramontana, M.: Evolutionary geological models of the central-western peri-Mediterranean chains: a review, *Int. Geol. Rev.*, 128, 29–43, <https://doi.org/10.1080/00206814.2019.1706056>, 2021.
- Helmy, H. M., Botcharnikov, R., Ballhaus, C., Deutsch-Semlitskaya, A., Wirth, R., Schreiber, A., Buhre, S., and Häger, T.: Evolution of magmatic sulfide liquids: how and when base metal sulfides crystallize?, *Contrib. Miner. Petrol.*, 176, 107, <https://doi.org/10.1007/s00410-021-01868-4>, 2021.
- Hernáiz Huertas, P. P., García de Domingo, A., González Lasta, J., Zazo Cardeña, C., and Goy Goy, J. L.: Hoja Alcalá de los Gazules (no. 1070), Mapa Geológico de España 1 : 50 000, Segunda serie, I.G.M.E., Madrid, M-10375-1991, 1984.
- Holwell, D. A., Adeyemi, Z., Ward, L. A., Smith, D. J., Graham, S. D., McDonald, I., and Smith, J. W.: Low temperature alteration of magmatic Ni-Cu-PGE sulfides as a source for hydrothermal Ni and PGE ores: A quantitative approach

- using automated mineralogy, *Ore Geol. Rev.*, 91, 718–740, <https://doi.org/10.1016/j.oregeorev.2017.08.025>, 2017.
- Holness, M. B., Richardson C., and Helz, R. T.: Disequilibrium dihedral angles in dolerite sills: a new proxy for cooling rate, *Geology*, 40, 795–798, <https://doi.org/10.1130/G33119.1>, 2012.
- Ihlenfeld, C. and Keays, R. R.: Crustal contamination and PGE mineralization in the Platreef, Bushveld Complex, South Africa: evidence for multiple contamination events and transport of magmatic sulphides, *Mineral. Depos.*, 46, 813–832, <https://doi.org/10.1007/s00126-011-0340-0>, 2011.
- Jochum, K. P., Weis, U., Schwager, B., Stoll, B., Wilson, S. A., Haug, G. H., Andreae, M. O., and Enzweiler, J.: Reference Values Following ISO Guidelines for Frequently Requested Rock Reference Materials, *Geostand. Geoanal. Res.*, 40, 333–350, <https://doi.org/10.1111/j.1751-908X.2015.00392.x>, 2016.
- Kanitpanyacharoen, W. and Boudreau, A. E.: Sulfide-associated mineral assemblages in the Bushveld Complex, South Africa: Platinum-group element enrichment by vapor refining by chloride-carbonate fluids, *Mineral Depos.*, 48, 193–210, <https://doi.org/10.1007/s00126-012-0427-2>, 2012.
- Kelly, D. P. and Vaughan, J. D.: Pyrrhotine-pentlandite ore textures: a mechanistic approach, *Mineral. Mag.*, 47, 453–463, <https://doi.org/10.1180/minmag.1983.047.345.06>, 1983.
- Kihara, K.: An x-ray study of the temperature dependence of the quartz structure, *Eur. J. Mineral.*, 2, 63–77, <https://doi.org/10.1127/ejm/2/1/0063>, 1990.
- Kitakaze, A., Machida, T., and Komatsu, R.: Phase relations in the Fe-Ni-S system from 875 to 650 °C, *Can. Mineral.*, 54, 1175–1186, <https://doi.org/10.3749/canmin.1500087>, 2016.
- Klein, E. M.: Geochemistry of the Igneous Oceanic Crust, in: *Treatise on Geochemistry*, Vol. 3. The Crust, edited by: Holland, H. D. and Turekian, K. K., Elsevier, 433–463, <https://doi.org/10.1016/B0-08-043751-6/03030-9>, 2003.
- Klemm, D. D.: Synthesen und Analysen in den Dreiecks diagrammen FeAsS–CoAsS–NiAsS und FeS₂–CoS₂–NiS₂, *Neues Jahrb. Mineral. Abh.*, 103, 205–255, 1965.
- Knight, K. S., Marshall, W. G., and Zochowski, S. W.: The low temperature and high-pressure thermoelastic and structural properties of chalcopyrite, CuFeS₂, *Can. Mineral.*, 49, 1015–1034, <https://doi.org/10.3749/canmin.49.4.1015>, 2011.
- Korneeva, A. A., Nekrylov, N., Kamenetsky, V. S., Portnyagin, M. V., Savelyev, D. P., Krasheninnikov, S. P., Abersteiner, A., Kamenetsky, M. B., Zelenski, M. E., Shcherbakov, V. D., and Botcharnikov, R. E.: Composition, crystallization conditions and genesis of sulfide-saturated parental melts of olivine-phyric rocks from Kamchatsky Mys (Kamchatka, Russia), *Lithos*, 370/371, 105657, <https://doi.org/10.1016/j.lithos.2020.105657>, 2020.
- Kovalenko, V. I., Naumov, V. B., Girmis, A. V., Dorofeeva, V. A., and Yarmolyuk, V. V.: Average compositions of magmas and mantle sources of mid-ocean ridges and intraplate oceanic and continental settings estimated from the data on melt inclusions and quenched glasses of basalts, *Petrology*, 15, 335–368, <https://doi.org/10.1134/S0869591107040029>, 2007.
- Kullerud, G. and Yoder, H. S.: Pyrite stability relations in the Fe-S system, *Econom. Geol.*, 54, 533–572, <https://doi.org/10.2113/gsecongeo.54.4.533>, 1959.
- Kullerud, G. and Yund, R. A.: The Ni-S system and related minerals, *J. Petrol.*, 3, 126–175, <https://doi.org/10.1093/petrology/3.1.126>, 1962.
- Kusebauch, C., Oelze, M., and Gleeson, S. A.: Partitioning of arsenic between hydrothermal fluid and pyrite during experimental siderite replacement, *Chem. Geol.*, 500, 136–147, <https://doi.org/10.1016/j.chemgeo.2018.09.027>, 2018.
- Li, C. and Ripley, E. M.: Sulfur Contents at Sulfide-Liquid or Anhydrite Saturation in Silicate Melts: Empirical Equations and Example Applications, *Econ. Geol.*, 104, 405–412, <https://doi.org/10.2113/gsecongeo.104.3.405>, 2009.
- Li, C., Barnes, S. J., Makovicky, E., Rose-Hansen, J., and Makovicky, M.: Partitioning of nickel, copper, iridium, rhodium platinum and palladium between monosulfide solid solution and sulfide liquid: effects of composition and temperature, *Geochim. Cosmochim. Ac.*, 60, 1231–1238, [https://doi.org/10.1016/0016-7037\(96\)00009-9](https://doi.org/10.1016/0016-7037(96)00009-9), 1996.
- Liu, K., Zhang, L., Guo, X., and Ni, H.: Effects of sulfide composition and melt H₂O on sulfur content at sulfide saturation in basaltic melts, *Chem. Geol.*, 559, 119913, <https://doi.org/10.1016/j.chemgeo.2020.119913>, 2021.
- Mansur, E. T., Barnes, S. J., and Duran, C.: Textural and compositional evidence for the formation of pentlandite via peritectic reaction: implications for the distribution of highly siderophile elements, *Geology*, 47, 351–354, <https://doi.org/10.1130/G45779.1>, 2019.
- Mansur, E. T., Barnes, S. J., and Filho, C. F. F.: The effects of post-cumulus alteration on the distribution of chalcophile elements in magmatic sulphide deposits and implications for the formation of low-S-high-PGE zones: The Luanga deposit, Carajás Mineral Province, *Can. Mineral.*, 59, 1453–1484, <https://doi.org/10.3749/canmin.2100018>, 2021.
- Mansur, E. T., Slagstad, T., Dare, S. A. S., and Sandstad, J. S.: Geology and sulphide geochemistry of the Ni-Cu-Co mineralisation of the Espedalen Complex, Norway: Constraints for the distribution of magmatic sulphides within a variably deformed anorthosite suite, *Ore Geol. Rev.*, 161, 105666, <https://doi.org/10.1016/j.oregeorev.2023.105666>, 2023.
- Martín-Algarra, A.: Evolución geológica alpina del contacto entre las Zonas Internas y las Zonas Externas de la Cordillera Bética [Ph.D.], Universidad de Granada, Spain, 1171 pp., <http://hdl.handle.net/10481/75699> (last access: 17 March 2025), 1987.
- Marzoli, A., Renne, P. R., Piccirillo, E. M., Ernesto, M., Bellieni, G., and DeMin, A.: Extensive 200 million years old continental flood basalts from the Central Atlantic Magmatic Province, *Science*, 248, 616–618, <https://doi.org/10.1126/science.284.5414.616>, 1999.
- McDonough, W. F. and Sun, S. S.: The composition of the Earth, *Chem. Geol.*, 120, 223–253, [https://doi.org/10.1016/0009-2541\(94\)00140-4](https://doi.org/10.1016/0009-2541(94)00140-4), 1995.
- McDonald, I. and Holwell, D. A.: Did lower zone magma conduits store PGE-rich sulfides that were later supplied to the Platreef?, *S. Afr. J. Geol.*, 110, 611–616, 2007.
- McDonald, I., Holwell, D. A., and Wesley, B.: Assessing the Potential Involvement of an Early Magma Staging Chamber in the Generation of the Platreef Ni-Cu-PGE Deposit in the Northern Limb of the Bushveld Complex: A Pilot Study of the Lower Zone Complex at Zwartfontein, *Appl. Earth Sci.*, 118, 5–20, <https://doi.org/10.1179/174327509X434902>, 2009.
- Morata, D.: Petrología y geoquímica de las ofitas de las zonas externas de las Cordilleras Béticas [Ph.D.], Instituto Andaluz de Ge-

- ología Mediterránea, Spain, 342 pp., <http://hdl.handle.net/10481/54267> (last access: 17 March 2025), 1993.
- Morata, D. and Puga, E.: Los piroxenos de las doleritas triasicas de las Zonas Externas de las Cordilleras Beticas como indicadores petrogeneticos, *Bol. Soc. Esp. Min.*, 15, 175–187, 1991.
- Morata, D. and Puga, E.: Aluminium silicate xenocrystals in the “ophites” of the Subbetic Zone (Southern Spain), *Schw. Mineral. Petr. Mitt.*, 72, 379–387, 1992.
- Morata, D., Puga, E., and Aguirre, L.: Very low-grade metamorphism of Triassic dolerites from the Archidona region, Subbetic Cordillera, Spain, *JGCP*, 294, Davis, California (USA), abstract, 1992.
- Morata, D., Puga, E., Demant, A., and Aguirre, L.: Geochemistry and tectonic setting of the “ophites” from the external zones of the Betic Cordilleras (southern Spain), *Estud. Geol.*, 53, 107–120, 1997.
- Morata, D., Aguirre, L., and Puga, E.: Na-metamorphic pyroxenes in low-grade metabasites from the External Zones of the Betic Cordilleras (Southern Spain): influence of rock-chemical composition on their formation, *Rev. Soc. Geol. Chile*, 21, 3–17, 1994.
- Morimoto, N., Nakazawa, H., Nishiguchi, K., and Tokonami, M.: Pyrrhotites: Stoichiometric compounds with composition $Fe_{n-1}S_n$ ($n \geq 8$), *Science*, 168, 964–966, <https://doi.org/10.1126/science.168.3934.964>, 1970.
- Morimoto, N., Fabries, J., Ferguson, A. K., Ginzburg, I. V., Ross, M., Seifert, F. A., Zussman, J., Aoki, K., and Gottardi, G.: Nomenclature of pyroxenes, *Am. Mineral.*, 73, 1123–1133, 1988.
- Mountain, B. W. and Seward, T. M.: Hydrosulfide/sulfide complexes of copper(I): Experimental confirmation of the stoichiometry and stability of $Cu(HS)_2$ at temperatures, *Geochim. Cosmochim. Ac.*, 67, 3005–3014, [https://doi.org/10.1016/S0016-7037\(03\)00303-X](https://doi.org/10.1016/S0016-7037(03)00303-X), 2003.
- Mungall, J., Andrews, D. R., Cabri, L. J., Sylvester, P., and Rubrett, M.: Partitioning of Cu, Ni, Au, and platinum-group elements between monosulfide solid solution and sulfide under controlled oxygen and sulfur fugacities, *Geochim. Cosmochim. Ac.*, 69, 4349–4360, <https://doi.org/10.1016/j.gca.2004.11.025>, 2005.
- Mungall, J., Brenan, J. M., Godel, B., Barnes, S. J., and Gailard, F.: Transport of metals and sulphur in magmas by flotation of sulphide melt on vapour bubbles, *Nat. Geosci.*, 8, 216–219, <https://doi.org/10.1038/ngeo2373>, 2015.
- Murowchick, J. B.: Marcasite inversion and the petrographic determination of pyrite ancestry, *Econ. Geol.*, 87, 1141–1152, <https://doi.org/10.2113/gsecongeo.87.4.1141>, 1992.
- Nagai, T., Kagai, H., and Yamanaka, T.: Variation of hydrogen bonded O...O distances in goethite at high pressure, *Am. Mineral.*, 88, 1423–1427, <https://doi.org/10.2138/am-2003-1005>, 2003.
- Naldrett, A. J.: Magmatic sulfide deposits: Geology, Geochemistry and Exploration, <https://doi.org/10.1007/978-3-662-08444-1>, 2004.
- Naldrett, A. J. and Kullerud, G.: A study of the Strathcona mine and its bearing on the origin of nickel-copper ores of the Sudbury district, Ontario, *J. Petrol.*, 8, 453–531, <https://doi.org/10.1093/petrology/8.3.453>, 1967.
- Naldrett, A. J., Craig, J. R., and Kullerud, G.: The central portion of the Fe–Ni–S system and its bearing on pentlandite exsolution in iron nickel sulfide ores, *Econ. Geol.*, 62, 826–847, <https://doi.org/10.2113/gsecongeo.62.6.826>, 1967.
- Naldrett, A. J., Lehmann, J., and Augé, T.: Spinel non-stoichiometry and reactions between chromite and closely associated sulphides, with examples from ophiolite complexes, in: *Magmatic Sulphides – The Zimbabwe volume*, edited by: M. D. Predergast, J. Jones, The Institution of Mining and Metallurgy, London, 221–227, <https://doi.org/10.3749/canmin.49.6.1571>, 1989.
- Naldrett, A. J., Kinnaird, J., Wilson, A., Yudovskaya, M., McQuade, S., Chunnnett, G., and Stanley, C.: Chromite composition and PGE content of Buhsveld chromitites: Part 1 – the lower and middle groups, *Trans.-Inst. Min. Metall., Sect. C*, 118, 131–161, 2009.
- Neyedley, K., Hanley, J. J., Falck, H., Bodnar, R. J., Fedele, L., Fayek, M., and Sharpe, R.: Sulfide melt inclusions associated with magmatic Ni-Cu-platinum-group element (PGE) mineralization in the Caribou Lake Gabbro, Blatchford Lake intrusive suite, Northwest Territories, Canada, *Ore Geol. Rev.*, 107, 513–531, <https://doi.org/10.1016/j.oregeorev.2019.02.009>, 2019.
- Norman, M., Garcia, M. O., and Pietruszka, A. J.: Trace-element distribution coefficients for pyroxenes, plagioclase, and olivine in evolved tholeiites from the 1955 eruption of Kilauea Volcano, Hawaii, and petrogenesis of differentiated rift-zone lavas, *Am. Mineral.*, 90, 888–899, <https://doi.org/10.2138/am.2005.1780>, 2005.
- Nowack, E., Schwarzenbach, D., Gonschorek, W., and Hahn, T.: Deformationsdichten in CoS_2 und NiS_2 mit pyritstruktur, *Z. Kristallogr.*, 186, 213–215, 1989.
- Paton, C., Hellstrom, J., Paul, B., Woodhead, J., and Hergt, J.: Iolite: Freeware for the visualisation and processing of mass spectrometry data, *J. Anal. Atom. Spectrom.*, 26, 2508–2518, <https://doi.org/10.1039/C1JA10172B2011>.
- Peregoedova, A. V. and Ohnenstetter, M.: Collectors of Pt, Pd and Rh in a S-poor Fe–Ni–Cu–sulfide system at 760 °C: experimental data and application to ore deposits, *Can. Mineral.*, 40, 527–561, <https://doi.org/10.2113/gscanmin.40.2.527>, 2002.
- Pérez-López, A., Cambeses, A., Pérez-Valera, F., and Götz, A. E.: Rhaetian tectono-magmatic evolution of the Central Atlantic Magmatic Province volcanism in the Betic Cordillera, South Iberia, *Lithos*, 396–397, 106230, <https://doi.org/10.1016/j.lithos.2021.106230>, 2021.
- Pérez-López, A. and Pérez-Valera, F.: Palaeogeography, facies and nomenclature of the Triassic units in the different domains of the Betic Cordillera (S Spain), *Palaeogeogr. Palaeoclimatol.*, 254, 606–626, <https://doi.org/10.1016/j.palaeo.2007.07.012>, 2007.
- Pérez-Valera, F. and Pérez-López, A.: Stratigraphy and sedimentology of Muschelkalk carbonates of the Southern Iberian Continental Palaeomargin (Siles and Cehégín Formations, Southern Spain), *Facies*, 54, 61–87, <https://doi.org/10.1007/s10347-007-0125-1>, 2008.
- Pérez-Valera, F., Sánchez-Gómez, M., Pérez-López, A., and Pérez-Valera, L. A.: An evaporite-bearing accretionary complex in the northern front of the Betic-Rif orogeny, *Tectonics*, 36, 1006–1036, <https://doi.org/10.1002/2016TC004414>, 2017.
- Piña, R. (Eds.): *The Ni-Cu-(PGE) Aguablanca Ore Deposit (SW Spain)*, Springer Briefs in World Mineral Deposits, 78 pp., <https://doi.org/10.1007/978-3-319-93154-8>, 2019.
- Piña, R., Gervilla, F., Barnes, S. J., Ortega, L., and Lunar, R.: Platinum group elements-bearing pyrite from the Aguablanca

- Ni-Cu sulphide deposit (SW Spain): a LA-ICP-MS study, *Eur. J. Mineral.*, 25, 241–252, <https://doi.org/10.1127/0935-1221/2013/0025-2290>, 2013.
- Pokrovski, G. S., Blanchard, M., Saunier, G., and Poitrasson, F.: Mechanisms and rates of pyrite formation from hydrothermal fluid revealed by iron isotopes, *Geochim. Cosmochim. Ac.*, 304, 281–304, <https://doi.org/10.1016/j.gca.2021.03.006>, 2021.
- Portugal-Ferreira, M., Morata, D., Puga, E., Demant, A., and Aguirre, L.: Evolución geoquímica y temporal del magmatismo básico mesozoico en las Zonas Externas de las Cordilleras Béticas, *Estud. Geol.*, 51, 109–118, <https://doi.org/10.3989/egol.1995>.
- Powell, A. V., Vaqueiro, P., Knight, K. S., Chapon, L. C., and Sanchez, R. D.: Structure and magnetism in synthetic pyrrhotite Fe₇S₈: A powder neutron-diffraction study, *Phys. Rev. B*, 70, 014415–12, <https://doi.org/10.1103/PhysRevB.70.014415>, 2004.
- Puga, E., Morten, L., Bondi, M., Bargossi, J., and Ruiz-Cruz, M. D., Díaz de Federico, A.: Metamorphosed “ophites” from the Archidona region, Subbetic Zone (Spain), *Estudios Geol.*, 39, 307–317, 1983.
- Puga, E., Van de Fliert, J. R., Torres Roldan, R. L., and Sanz de Galdeano, C.: Attempts of whole-rock K / Ar dating of Mesozoic volcanic and hypabissal igneous rocks from the Central Subbetic (Southern Spain): A case of differential Argon loss related to very low-grade metamorphism, *Estud. Geol.*, 44, 47–59, <https://doi.org/10.3989/egol.88441-2523>, 1988.
- Puga, E., Díaz de Federico, A., Fanning, C. M., Nieto, J. M., Rodríguez Martínez-Conde, A. J., Díaz-Puga, M. A., Lozano, J. A., Bianchini, G., Natali, C., and Beccaluva, L.: The Betic Ophiolites and the Mesozoic Evolution of the Western Tethys, *Geosciences*, 7, 31, <https://doi.org/10.3390/geosciences7020031>, 2017.
- Qian, G., Xia, F., Brugger, J., Skinner, W. M., Bei, J., Chen, G., and Pring, A.: Replacement of pyrrhotite by pyrite and marcasite under hydrothermal conditions up to 220 °C: An experimental study of reaction textures and mechanisms, *Am. Mineral.*, 96, 1878–1893, <https://doi.org/10.2138/am.2011.3691>, 2011.
- Rajamani, V. and Prewitt, C. T.: Crystal chemistry of natural pentlandites, *Can. Mineral.*, 12, 178–187, 1973.
- Ray, D., Mevel, C., and Banerjee, R.: Hydrothermal alteration studies of gabbros from Northern Central Indian Ridge and their geodynamic implications, *J. Earth Syst. Sci.*, 118, 659–676, <https://doi.org/10.1007/s12040-009-0055-0>, 2009.
- Rickard, D. and Cowper, M.: Kinetics and mechanism of chalcopyrite formation from Fe(II) disulphide in aqueous solution (< 200 °C), *Geochim. Cosmochim. Ac.*, 58, 3795–3802, [https://doi.org/10.1016/0016-7037\(94\)90364-6](https://doi.org/10.1016/0016-7037(94)90364-6), 1994.
- Rickard, D. and Luther, G. W. III: Kinetics of pyrite formation by the H₂S oxidation of iron (II) monosulfide in aqueous solutions Between 25 and 125 °C: The rate equation, *Geochim. Cosmochim. Ac.*, 61, 115–134, [https://doi.org/10.1016/S0016-7037\(96\)00322-5](https://doi.org/10.1016/S0016-7037(96)00322-5), 1997.
- Rickard, D. and Luther III, G. W.: Chemistry of iron sulfides, *Chem. Rev.*, 107, 514–522, 2007.
- Rieder, M., Crelling, J. C., Sustai, O., Drabek, M., Weiss, Z., and Klementova, M.: Arsenic in iron disulfides in a brown coal from the North Bohemian Basin, Czech Republic, *International J. Coal Geol.*, 71, 115–121, <https://doi.org/10.1016/j.coal.2006.07.003>, 2007.
- Ripley, E. M. and Li, C.: Sulfide saturation in mafic magmas: is external sulfur required for magmatic Ni-Cu-(PGE) ore genesis?, *Econ. Geol.*, 108, 45–58, <https://doi.org/10.2113/econgeo.108.1.45>, 2013.
- Rodríguez-Cañero, R., Jabaloy-Sánchez, A., Navas-Parejo, P., and Martín-Algarra, A.: Linking Palaeozoic palaeogeography of the Betic cordillera to the Variscan Iberian Massif: new insight through the first conodonts of the Nevado-Filábride complex, *Int. J. Earth Sci.*, 107, 1791–1806, <https://doi.org/10.1007/s00531-017-1572-8>, 2018.
- Rosebaum, G., Lister, G., and Duboz, C.: Reconstruction of the tectonic evolution of the Western Mediterranean since the Oligocene, *J. Virt. Explor.*, 8, 107–130, <https://doi.org/10.3809/jvirtex.2002.00053>, 2002.
- Sanz de Galdeano, C., El Kadiri, K., Simancas, F., Rachid, H., López-Garrido, A. C., El Mrihi, A., and Chalouan, A.: Paleogeographical reconstruction of the Malaguide-Ghomaride Complex (Internal Betic-Rifian Zone) based on Carboniferous granitoid pebble provenance, *Geol. Carpath.*, 57, 327–336, 2006.
- Schmid-Beurmann, P. and Lottermoser, W.: ⁵⁷Fe-Moessbauer spectra, electronic and crystal structure of members of the CuS₂-FeS₂ solid solution series, *Phys. Chem. Mineral.*, 19, 571–577, <https://doi.org/10.1007/BF00203056>, 1993.
- Seat, Z., Beresford, S. W., Grguric, B. A., Gee, M. A. M., and Grassineau, N. V.: Reevaluation of the role of external sulfur addition in the genesis of Ni-Cu-PGE deposits: Evidence from the Nebo-Babel Ni-Cu-PGE deposit, West Musgrave, Western Australia, *Econ. Geol.*, 104, 521–538, <https://doi.org/10.2113/gsecongeo.104.4.521>, 2009.
- Smith, J., Graziane, R., Petts, D. C., and Regis, D.: Crystallographic controlled exsolution and metal partitioning in magmatic sulfide deposits, *Chemistry*, 83, 125954, <https://doi.org/10.1016/j.chemer.2023.125954>, 2023.
- Sugaki, A. and Kitakaze, A.: High form of pentlandite and its thermal stability, *Am. Mineral.*, 83, 133–140, <https://doi.org/10.2138/am-1998-1-213>, 1998.
- Sun, S. S. and McDonough, W. F.: Chemical and isotopic systematics of oceanic basalts: implications for mantle composition and processes, in: *Magmatism in the Ocean Basins*, Geological Society of London Special Publications, edited by: Saunders, A. D. and Norry, M. J., 313–345, <https://doi.org/10.1144/GSL.SP.1989.042.01.19>, 1989.
- Sun, Z., Xion, X., Wang, J., Liu, X., Ruan, L., Zhang, L., and Takakashi, E.: Sulfur abundance and heterogeneity in the MORB mantle estimated by copper partitioning and sulfur solubility modelling, *Earth Planet. Sc. Lett.*, 538, 116169, <https://doi.org/10.1016/j.epsl.2020.116169>, 2020.
- Tenailléau, C., Pring, A., Etschmann, B., Brugger, J., and Studer, A.: Transformation of pentlandite to violarite under mild hydrothermal conditions, *Am. Mineral.*, 91, 706–709, <https://doi.org/10.2138/am.2006.2131>, 2006.
- Tsujimura, T. and Kitakaze, A.: New Phase Relations in the Cu-Fe-S System at 800 °C; constraint of fractional crystallization of a sulfide liquid, *Neues Jahr Mineral. Monatsh.*, 10, 433–444, <https://doi.org/10.1127/0028-3649/2004/2004-0433>, 2004.
- Tsujimura, K., Nakazawa, H., Endo, T., and Fukunaga, O.: Cation distribution in Pentlandites (Fe,Ni)₉S₈: dependence of pressure and temperature and kinetics of the cation

- exchange reaction, *Phys. Chem. Miner.*, 19, 203–212, <https://doi.org/10.1007/BF00202309>, 1992.
- Vera, J. A. (Eds.): *Geología de España*, Sociedad Geológica de España e Instituto Geológico y Minero de España, Madrid, ISBN 84-7840-546-1, 2004.
- Waal, S. A.: Experimental simulation of the supergene reaction: pyrrhotite \rightarrow marcasite + Fe^{3+} + electrons, *Trans. Geol. Soc. S. Afr.*, 87, 273–279, 1984.
- Wang, H. and Salveson, I.: A review on the mineral chemistry of the nonstoichiometric iron sulphide, Fe_{1-x}S ($0 \leq x \leq 0.125$): polymorphs, phase relations and transitions, electronic and magnetic structures, *Phase Trans.*, 78, 547–567, <https://doi.org/10.1080/01411590500185542>, 2005.
- Wang, H., Pring, A., Ngothai, Y., and O'Neill, B.: The kinetics of the $\alpha \rightarrow \beta$ transition in synthetic nickel monosulfide, *Am. Mineral.*, 91, 171–181, <https://doi.org/10.2138/am.2006.1962>, 2006.
- Wang, S. M., Wu, C. Z., Muntar, M. N., Lei, R. X., and Brzozowski, M. J.: Mobilization of ore-forming metals during post-magmatic hydrothermal overprinting of the Huangshandong Ni–Cu sulfide deposit, Eastern Tianshan, NW China, *Ore Geol. Rev.*, 137, 104315, <https://doi.org/10.1016/j.oregeorev.2021.104315>, 2021.
- Winchester, J. A. and Floyd, P. A.: Geochemical discrimination of different magma series and their differentiation products using immobile elements, *Chem. Geol. J.*, 20, 325–343, [https://doi.org/10.1016/0009-2541\(77\)90057-2](https://doi.org/10.1016/0009-2541(77)90057-2), 1977.
- Xia, F., Brugger, J., Chen, G. R., Ngothai, Y., O'Neill, B., Putnis, A., and Pring, A.: Mechanism and kinetics of pseudomorphic mineral replacement reactions: A case study of the replacement of pentlandite by violarite, *Geochim. Cosmochim. Ac.*, 73, 1945–1969, <https://doi.org/10.1016/j.gca.2009.01.007>, 2009a.
- Yao, X., Xia, F., Deditius, A. P., Brugger, J., Etschmann, B. E., and Pearce, M. A.: The Mechanism and Kinetics of the Transformation from Marcasite to Pyrite: In Situ and Ex Situ Experiments and Geological Implications, *Contrib. Mineral. Petrol.*, 175, 27, <https://doi.org/10.1007/s00410-020-1665-4>, 2020.
- Yao, X., Xia, F., Brugger, J., Kartal, M., and Adegoke, I. A.: Rapid Marcasite to Pyrite Transformation in Acidic Low-Temperature Hydrothermal Fluids and Saturation Index Control on FeS_2 Precipitation Dynamics and Phase Selection, *ACS Earth Space Chem.*, 5, 2453–2465, <https://doi.org/10.1021/acsearthspacechem.1c00137>, 2021.
- Yücel, M., Gartman, A., Chan, C., and Luther III, G. W.: Hydrothermal vents as a kinetically stable source of iron-sulphide-bearing nanoparticles to the ocean, *Nat. Geosci.*, 4, 367–371, <https://doi.org/10.1038/ngeo1148>, 2011.
- Yund, R. A. and Kullerud, G.: Thermal stability of assemblages in the Cu-Fe-S system, *J. Petrol.*, 7, 454–488, <https://doi.org/10.1093/petrology/7.3.454>, 1966.
- Zhang, Y., Li, W., Cai, Y., Qu, Y., Pan, Y., Zhang, W., and Zhao, K.: Experimental investigation of the reactions between pyrite and aqueous Cu(I) chloride solution at 100–250 °C, *Geochim. Cosmochim. Ac.*, 298, 1–20, <https://doi.org/10.1016/j.gca.2021.01.018>, 2021.